J. Fluid Mech. (1994), vol. 262, pp. 223–263

Pressure fluctuations and their effect on cavitation inception within water jets

By BING RAN AND JOSEPH KATZ
Department of Mechanical Engineering, The Johns Hopkins University, Baltimore, MD 21218, USA

(Received 26 February 1993 and in revised form 6 September 1993)

Instantaneous and phase averaged pressure distributions in the near field of a jet, and their effects on the conditions for the onset of cavitation are studied in detail. The measurements are performed by using microscopic bubbles as pressure sensors, and holography as a means of detecting them. Experiments are performed at Re_d exceeding 4×10^5, with and without acoustic excitation. The results show that the highest negative pressure peaks (-0.97) and the resulting cavitation inception occur because of vortex pairing. Prior to pairing the negative peaks are between -0.8 and -0.9. Weak acoustic excitation changes the entire flow structure and the spatial distributions of bubbles, but has little effect on the onset of cavitation. Downstream of the potential core the highest pressure peaks (~ -0.6) are considerably smaller, in agreement with the occurrence of cavitation there. It is also shown that although the r.m.s. values of pressure fluctuations do not vary with the jet speed, the probability distribution changes significantly, causing a reduction in the inception index with increasing velocity. The probability of cavitation inception is estimated from the distributions of bubbles and pressure peaks. It is shown that the actual, non-uniform bubble distribution increases the probability of inception owing to migration of the bubbles to the low pressure regions.

1. Introduction

1.1. Background

It is already well established, that the onset of vaporous cavitation involves an unstable growth and collapse of a microscopic nucleus, as a result of exposure to a low pressure (see Arndt 1981 for an extensive summary). Thus, predictions of the conditions for cavitation inception require knowledge of the types, sizes and spatial distributions of nuclei, as well as detailed information on the pressure field. Unfortunately, researchers have encountered major difficulties in both areas. It is difficult to measure the distributions of nuclei, and in many cases, it is not clear whether they are bubbles, solid particles or a combination of both. When the nucleus is a spherical bubble located within an infinite medium, the condition for instability is:

$$P_\infty - P_v = -\frac{4s}{3R}, \tag{1}$$

where P_∞ and P_v are the ambient and vapour pressures, respectively, R is the bubble radius, and s is the surface tension. When the nucleus is a solid particle, or when the bubble is located in a turbulent flow field, the conditions for instability are considerably more complicated (e.g. Ramani & Chahine 1992). In a few studies in which the nuclei distributions were measured and the pressure was known (attached flows around smooth bodies), the measurements agreed only qualitatively with predicted rates of cavitation events (Meyer, Billet & Holl 1992; Ceccio & Brennen 1991).

Measurement of free-stream pressure fluctuations within turbulent flows is a difficult task. Most of the past experiments have been performed with intrusive fixed probes (George, Beuther & Arndt 1984; Arndt & George 1978; Fuchs 1972), and as a result are prone to errors (Willmarth 1975), especially at high frequencies, and particularly when the desired data extend beyond spectral distributions and r.m.s. values. A potential solution to this problem, involving use of microscopic bubbles as pressure sensors, was introduced first by Ooi & Acosta (1983). They seeded the near field of a jet with bubbles of known size, and determined the instantaneous pressure by measuring the bubble diameter. Since their sensors moved 'randomly' in space, they recorded holograms of the flow field, and performed measurements within the reconstructed images. Their limited database, random recording procedures and small jet diameters (3–6 mm), prevented them from identifying which flow phenomena were responsible for the pressure peaks. However, they did open the way for a possible approach to identify, measure and explain the conditions for cavitation inception in turbulent flows. Similar procedures were used by O'Hern (1987), while studying the pressure field behind a sharp edge plate, and by Green (1988), while studying tip vortices. In both cases the pressure measurements were limited, owing to seeding difficulties.

By measuring the bubble diameter, Ooi & Acosta actually determined the changes in the density of gas within the bubble, assuming that mass diffusion was insignificant. They did not calibrate the bubble response, and as a result had to assume a polytropic constant, relating between the pressure and the density. As they observed, the results depended strongly on their choice of a polytropic constant, and consequently they could not provide definite answers on the magnitude of pressure peaks. This problem was resolved by Ran & Katz (1991), who performed a series of calibration experiments with bubbles containing different gases. They confirmed that for a timescale, T, satisfying

$$T \gg \frac{R^2}{\alpha}, \tag{2}$$

where α is the thermal diffusivity of the gas, the bubble response was isothermal. This study showed also that for the same timescales mass diffusion affected the size of CO_2 bubbles, but had negligible effect on the responses of Air, H_2 and He bubbles. The large ratio between thermal and mass diffusion coefficients (about 10000:1), and the relatively low solubility of the latter gases, were the primary reason that bubbles could reach thermal equilibrium, with insignificant mass diffusion. To ensure that gas diffusion into the bubble was insignificant, the calibration experiments were extended to timescales, that were an order of magnitude longer than any scale relevant to the present study.

1.2. *Bubbles as pressure sensors*

For reliable free-stream pressure measurements within a turbulent flow field, the sensor must be considerably smaller than significant flow structures, and its response time must be considerably shorter than the characteristic timescale associated with this flow. As long as the resonant frequency of this sensor is much higher (by at least an order of magnitude) than the frequency of pressure fluctuations, one can assume that the response is linear and essentially instantaneous (negligible phase lag). The natural frequency, ω_0, of a spherical bubble can be determined from a small perturbation analysis to the Rayleigh–Plesset equation (Plesset & Prosperetti 1977). The resulting expression is:

$$\omega_0 = \left[\frac{3P_{g0}}{\rho R_0^2} - \frac{2s}{\rho R_0^3}\right]^{\frac{1}{2}}. \tag{3}$$

The subscript '0' indicates initial or equilibrium conditions, P_{g0} is the partial pressure of gas within the bubble and ρ is the water density. At equilibrium the pressure–radius relationship is:

$$P_v - \frac{2s}{R_0} + P_{g0} = P_0, \tag{4}$$

and as a result the natural frequency is:

$$\omega_0 = \left[\frac{3}{\rho R_0^2}\left(P_0 - P_v + \frac{4s}{3R_0}\right)\right]^{\frac{1}{2}}. \tag{5}$$

Thus, the natural frequency of a 50 μm radius air bubble at atmospheric ambient pressure ($s = 72 \times 10^{-3}$ N m^{-1}) is about 3.5×10^5 rad s^{-1} (55 KHz). According to Fuchs (1972) and Arndt & George (1978), the peak Strouhal number, fd/V_j (f is the frequency, d is the jet diameter, and V_j is the velocity), of pressure fluctuations is about 0.5. Thus, at a velocity of 20 m s^{-1}, and a 2.5 cm diameter jet, the spectral peak is at 360 Hz. Note that this Strouhal number refers to Eulerian pressure fluctuations, and the pressure sensed by the bubble is closer to Lagrangian fluctuations (the bubble still slips). The frequency of significant fluctuations, however, extends to about 4 KHz. In this range a 50 μm radius bubble should be in equilibrium with its ambient, and (4) provides an accurate relationship between the pressure and bubble radius at any instant.

As noted before, the calibration experiments have demonstrated that the gas within the bubble responded isothermally. Thus, the partial pressure of gas at any instant can be determined from:

$$P_g = P_{g0}\left(\frac{R_0}{R}\right)^3, \tag{6}$$

and as a result, the instantaneous ambient pressure, P, is:

$$P = P_{g0}\left(\frac{R_0}{R}\right)^3 + P_v - \frac{2s}{R}. \tag{7}$$

Then, by using (4), one can obtain the simple expression,

$$P = \left(P_0 + \frac{2s}{R_0} - P_{v0}\right)\left(\frac{R_0}{R}\right)^3 - \frac{2s}{R} + P_v, \tag{8}$$

for the pressure, as a function of the instantaneous radius and some known reference conditions. The terms s and P_v are functions of temperature, and are assumed to be constant. Before concluding, note that, as long as cavitation does not occur, the high Weber number of a 50 μm radius air bubble in water prevents significant deformations in its shape. As will be demonstrated later, the extent of these deformations does not exceed 20–30% in extreme pressure gradients. In these cases it is still possible to determine the pressure from the bubble volume.

Ran & Katz (1991) also show that a train of uniform size bubbles (±2 μm) can be generated by stretching a capillary glass tube under heat until a nozzle, with a typical diameter of about 10 μm, is formed. Uncertainty analysis indicates that carefully

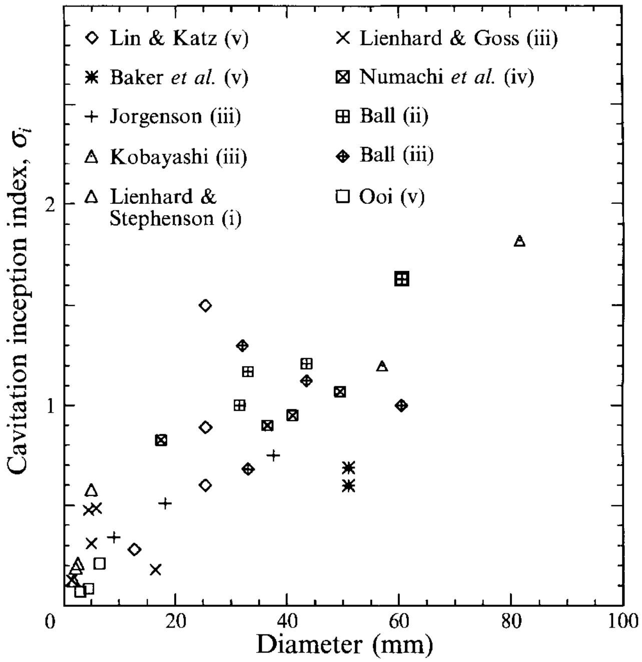

FIGURE 1. Collection of measured cavitation inception indices of water jets. Numbers indicate the following test arrangements: (i) Orifice in pipe, based on the pressure and velocity in the vena contracta. (ii) Orifice in pipe, based on the exit velocity, and pressure downstream. (iii) Standard smooth nozzle in pipe, based on the exit velocity and the pressure downstream. (iv) Orifice in pipe, based on the velocity and pressure in the vena contracta. (v) Nozzle in a large container.

performed experiment in flows with characteristic speeds of 20 m s^{-1} can resolve the pressure at an error level ranging between 6% and 10% of the dynamic head. Thus, microscopic bubbles can be used as pressure sensors, and can provide some answers on the conditions for cavitation inception in turbulent shear flows.

1.3. *Cavitation inception in water jets*

In spite of its significance, common occurrence, and the considerable effort invested in studying it, the conditions for cavitation inception in water jets are still unpredictable (see Baker, Holl & Arndt 1975; Arndt 1981). Figure 1 is a collection of measured cavitation inception indices, σ_i, defined as:

$$\sigma_i = \frac{P_{\infty i} - P_v}{\frac{1}{2}\rho V_j^2}, \tag{9}$$

where $P_{\infty i}$ is the ambient pressure during inception. The results vary between 0.1 and 1.6, and there is an apparent increase in σ_i with jet diameter. However, changes in the dissolved air content (i.e. concentration and size distributions of free-stream nuclei) and velocity in the same test facility can still cause variations between 0.3 and 1.6 (Lin & Katz 1988). The reported locations of inception within the jet also vary between 5 and 15 diameters downstream of the nozzle. They contradict the sites of maximum r.m.s. pressure fluctuations ($x/d < 3$) measured, for example, by Barefoot (1972). A possible reason for this discrepancy is the method used for detecting inception – visual observations under stroboscopic light, which is useful only when cavitation is already macroscopic. As the present paper shows, this crude measurement technique can lead to the wrong conclusion, since, as observed before in separated flows (Katz 1984), 'macroscopic cavitation' is preceded by 'microscopic cavitation' (intermittent cavitation involving bubbles with diameters less than about 1 mm). In fact, the earliest traces of explosive growth, collapse, and fragmentation of bubbles appear in the region of vortex pairing (in an unexcited jet), in complete agreement with the location of the highest pressure fluctuation peaks.

In an attempt to understand the causes and conditions for cavitation inception in jets, the present study focuses on measurements of pressure fluctuation, and on identification of specific flow phenomena causing them. Combined with measured (and discussed) spatial distributions of nuclei, the results are used for estimating the probability of cavitation inception.

2. Experiments

2.1. *Experimental set-up*

The experiments were performed in a high-speed jet facility, described schematically in figure 2(*a*). The 25.4 mm diameter jet was injected from a smooth, 4:1 diameter ratio, cosine shaped nozzle, that contained honeycombs and screens. The main test chamber was 1.98 m long and its cross-section was $0.69 \times 0.76\ m^2$. It had windows on all sides, which enabled observations to be made from any direction. The flow was driven by a 15 h.p. pump (located about 4 m below the nozzle in order to prevent pump cavitation), that enabled generation of up to 25–30 $m\ s^{-1}$ jets. An electromagnetic flow meter was used for measuring the flow rate. The ambient pressure was controlled by installing a smaller tank on top of the main chamber, keeping the water level at the middle of this tank, and connecting it to a vacuum pump and to a source of compressed air. Since a typical 20 $m\ s^{-1}$ jet already cavitated at atmospheric pressure, it was necessary to perform most experiments in a pressurized facility. The 32–38 mm thick windows enabled operation at ambient pressures up to 400 KPa. In some experiments the jet was acoustically excited by attaching a speaker to the pipe, and by adjusting the length of the pipe upstream of the nozzle to resonate (first mode) at the same frequency. A microphone attached to the nozzle confirmed that the entire piping system responded at a considerably higher amplitude when excited at the resonance modes.

The bubbles were injected from small nozzles made from capillary glass tubes, which were stretched under heat. A fine metering valve, air filters and pressure regulators were used for controlling the injection rate. In order to keep the injectors stable and generate a consistent bubble train, the injectors were attached to the honeycomb within the nozzle, and were kept outside of the boundary layer. As it turned out, this procedure enabled generation of uniform trains of bubbles that emerged, depending on the location of the injectors, between $r/d = 0$ and 0.4 (r is the radial distance from the centre of the jet, and d is the jet diameter). By keeping the bubbles within the potential core for a short time, it was also possible to obtain reference bubble sizes (R_0) and reference pressures (P_0).

The exact sizes and locations of bubbles were determined by using holography. The process consisted of recording holograms of the desired sample volume, reconstructing them and scanning the reconstructed image. In-line Fraunhofer holography was opted for, as sketched in figure 2(*b*) (see Collier, Burkhardt & Lin (1970) for background information). The light source of the holocamera was a pulsed ruby laser, capable of generating 25 mJ pulses with duration of about 25 ns. The laser output was spatially filtered, expanded to a 63 mm diameter beam, and collimated before illuminating the sample volume. Further increase in image quality was achieved by replacing the normal

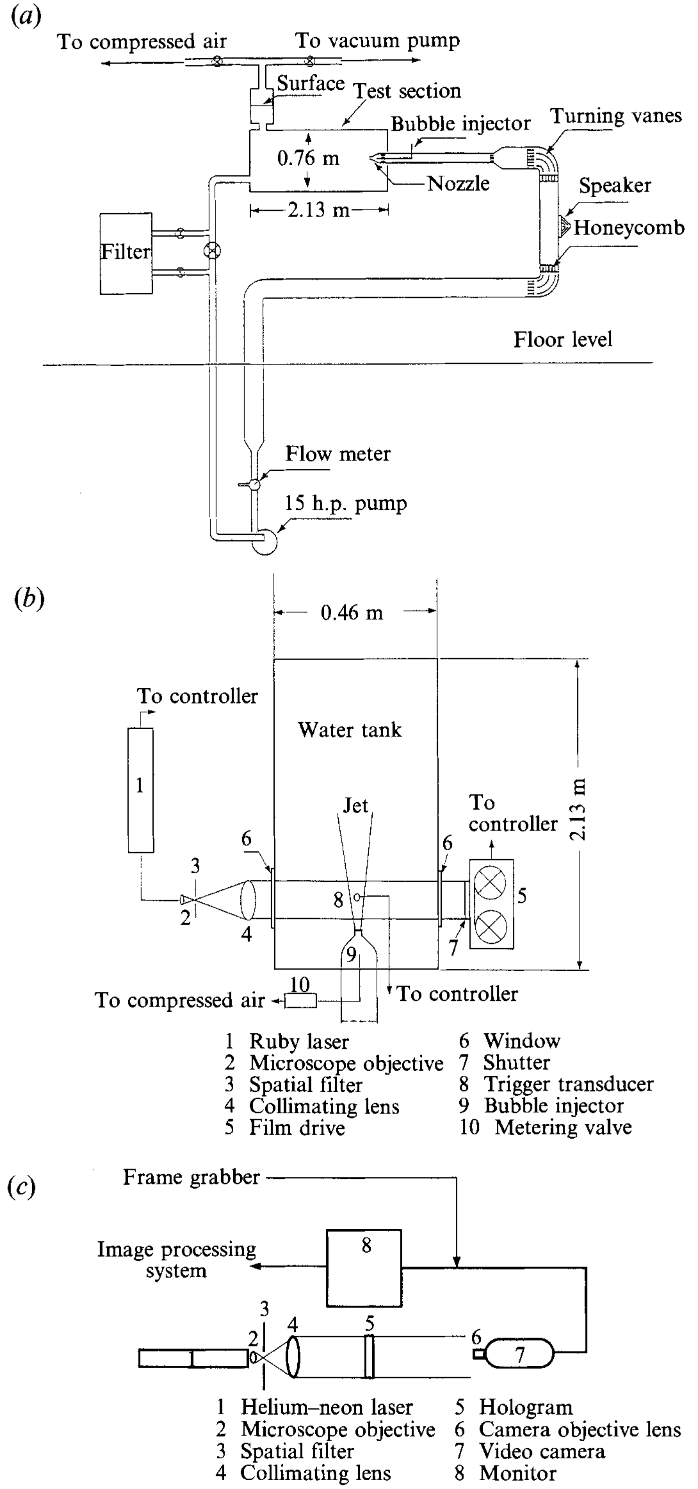

FIGURE 2. Schematic descriptions of the experimental facility. (*a*) High-speed jet facility. (*b*) Inline holocamera. (*c*) Reconstruction system.

lucite windows with polished glass windows in the region used for recording data. The holograms were recorded on a AGFA Gevaert 10E75, 70 mm film. Single exposure images were used for the pressure measurements in order to obtain the maximum possible resolution. Double exposure holograms, with delays ranging between 10 and 50 μs, were used only for determining the bubble velocity.

2.2. *Data analysis*

After being developed, each hologram was mounted on the reconstruction system (figure 2*c*) that used a He–Ne laser as a light source. Reconstruction with a He–Ne laser, that has a wavelength of 0.6328 μm, as opposed to the ruby's 0.6943 μm, does not change the lateral magnification of the image (Collier *et al.* 1970). However, the axial distance expands by a factor equal to the wavelength ratio, that is by 1.097 (in addition to differences in depth resulting from the refractive index of water). A video camera equipped with a microscope objective, capable of magnifying the image 500 times, was used for scanning the reconstructed image. The exact magnification was calibrated by recording holograms of microscope reticules. In order to improve our resolution and analysis procedures, the images were digitized at a magnification of 0.96 pixel μm^{-1} and enhanced. However, the bubble size was still determined manually, with the help of cursors. Attempts to obtain a better resolution with edge detection, etc. did not improve the resolution, owing to the presence of laser speckles, but helped in confirming the validity of the measurements. Based on careful evaluation of the entire process (Ran & Katz 1991), it was determined that the error in measuring the bubble diameter was about 2 μm.

During analysis the bubble diameters were determined at several orientations, and in most cases they remained spherical prior to the onset of cavitation (see sample in figure 3). Significant deviations from a spherical shape occurred only in a few cases, apparently due to bubble slip resulting from high local pressure gradients. As long as the deformations (differences between the major and minor axes) were in the order of 20–30 %, it was possible to estimate both the volume and the bubble slip velocity from its shape. The analysis involved an assumption that the bubble was a body of revolution, the minor axis being the axis of symmetry. Following several trials, it was concluded that in most cases the shape of the image could be replaced (curve fitted) with a sixth-order Legendre polynomial, as demonstrated in figure 4. Then, the volume of the bubble can be determined by simple integration. It is also possible to compute the potential flow around this body of revolution (figure 4*b*), with the slip velocity (u_s) as an unknown. By assuming that the internal pressure is constant (a reasonable assumption since the bubble contains gas), the shape of the bubble must be a direct result of surface tension response to differences in the local liquid pressure. Thus, the difference between the pressure at the leading-edge stagnation point (P_1), and the point of maximum velocity (P_2) is:

$$s\left(\frac{1}{R_2}+\frac{1}{R_2'}-\frac{2}{R_1'}\right)=P_1-P_2=\tfrac{1}{2}\rho u_s^2\left(\frac{u_2^2}{u_s^2}\right), \qquad (10)$$

where R_2' is half of the major axis, R_2' is the radius of curvature at the point of maximum velocity (u_2), and R_1' is the radius of curvature at the stagnation point. The ratio u_2^2/u_s^2 depends only on the shape of the bubble, namely on the coefficients of the Legendre polynomial replacing the bubble surface. Thus, it is possible to estimate the slip velocity from the shape of the bubble. This procedure was used in a few cses, and only for the purpose of demonstrating the effect of pressure gradients on bubble migration

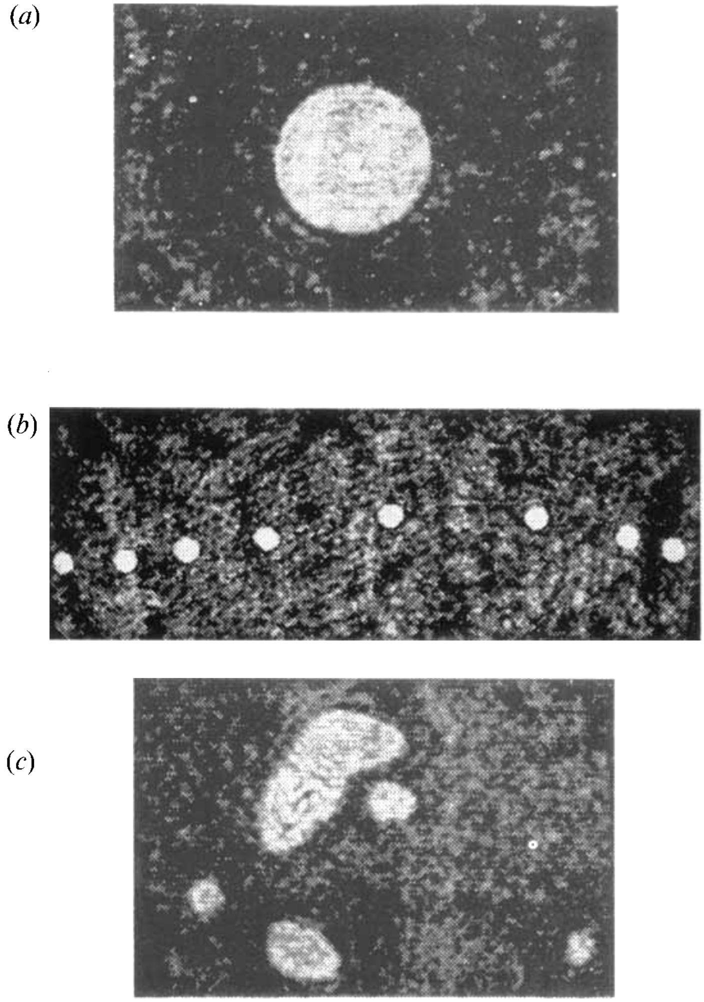

FIGURE 3. Samples of holographic images of bubbles. (*a*) A typical image of a 129 μm diameter spherical bubble. (*b*) A train of 120 μm diameter bubbles at a lower magnification. (*c*) A cluster of odd shaped bubbles during cavitation inception (bubbles are at different depths and cannot be focused simultaneously).

into the vortex core. Extreme cases, such as figure 4, occurred rarely, and mostly outside, but close to the core. For example, the bubble shown was located at $x/d = 2.5$ and $r/d = 0.73$, whereas the minimum pressure point was located at $x/d = 2.6$ and $r/d = 0.76$. The rest of the bubbles, including those that were located within the core (which were typically larger), remained spherical. The highest values of computed slip velocities extended up to about 10% of the local liquid velocity. Thus, slip due to pressure gradient was likely to have a significant effect on the spatial distribution of bubbles. As shown later in this paper, the bubble population in the vicinity of the vortex core was considerably higher than the average density, which increased the likelihood of cavitation inception.

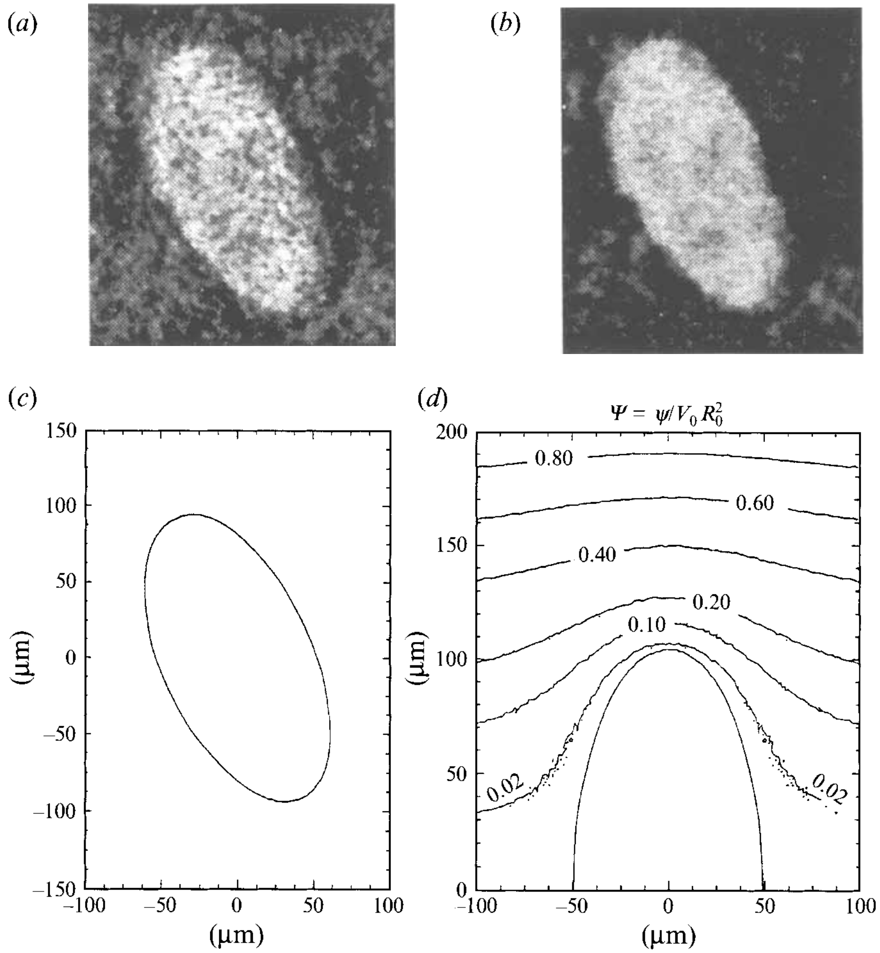

FIGURE 4. Computation of the potential flow around an actual bubble. (*a*) Original image of an elongated bubble during slip. (*b*) Same image after enhancement. (*c*) The shape of this bubble is fitted by a sixth-order Legendre polynomial. (*d*) Computed potential flow around this bubble.

2.3. *Experimental procedures*

The measurements had to be performed at an ambient pressure sufficiently high to prevent any cavitation inception, and the resulting unstable bubble response. Consequently, it was necessary to start the measurements by determining the conditions for cavitation inception, even in microscopic scales. This phase was performed by seeding the water with bubbles (ensuring that there were sufficient nuclei), and recording several holograms at different ambient pressures. The onset of cavitation was identified (figure 3*c*) by the appearance of a cluster of odd shaped bubbles with different sizes, and confirmed also by the spectra of a pressure transducer located inside the facility (a discussion follows).

Once the conditions for inception were determined and the pressure increased beyond that level, it was also necessary to ensure that all the 'pressure sensors' within the sample volume were generated by the bubble injectors. This problem required special measures for removal of free-stream bubbles, and operation at a dissolved air content of about 25–35 % of the saturation level (determined with an oxygen meter). Consequently, prior to an experiment the facility was maintained under heavy

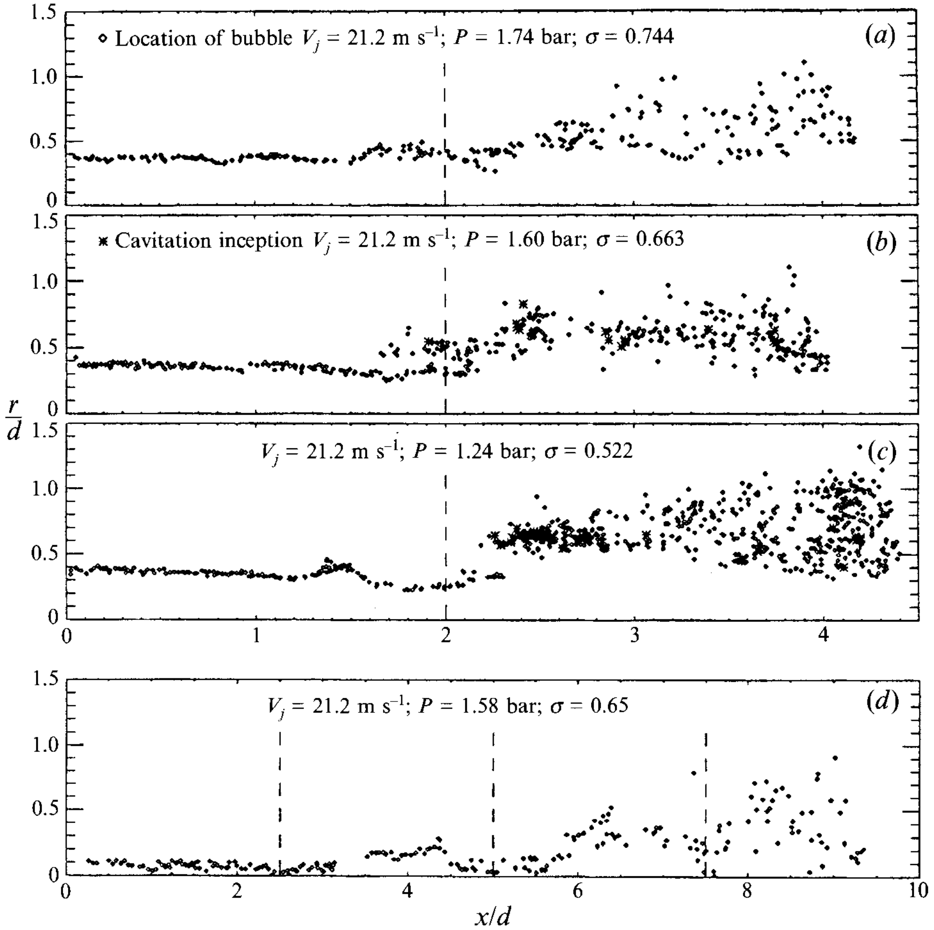

FIGURE 5. Instantaneous spatial distribution of bubbles injected from the nozzle at different cavitation indices. The jet velocity is 21.2 m s^{-1}. In (*a*), (*b*) and (*c*), the injector is located at $r/d = 0.4$; and in (*d*), it is at $r/d = 0$. Dashed lines indicate the extent of a single hologram.

cavitation (low pressure) for several hours, and then the pressure was increased for about an hour until the population of bubbles larger than 20 μm was essentially extinct. This procedure was repeated after several hours of experiments, as the population of free-stream bubbles recirculating in the main chamber, and accumulating near the top started increasing. Note also that the exit pipes from the main chamber (figure 2*a*) were installed close to the bottom of the facility in order to reduce the number of bubbles recirculating through the pump.

Relating the pressure distributions to the flow structure required a method for detecting the presence of a vortex, and triggering the holocamera when it reached a specific location. A simple solution was to install a piezoelectric pressure transducer (PCB model 102A05) within the facility, close to, but outside the jet (at $r/d = 1.5$ when $x/d = 1.25$ and 2.5), and use the negative peaks in its signal as an indicator of the exact time that a vortex passed by. As will be shown later, the transducer signal was also instrumental for detecting the occurrence of cavitation. Since the ruby laser was pumped by a flashlamp, two successive signals (negative peaks) were necessary for firing it; the first for triggering the flashlamp, and the second for activating the 'Q switch' (generating a laser pulse). The duration of each flash was about 1 ms, but

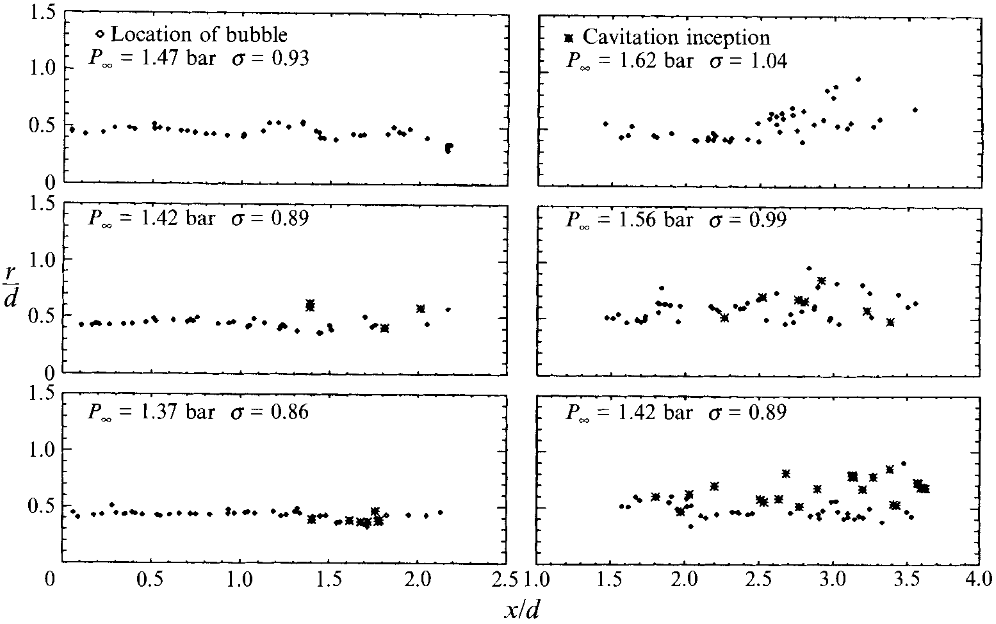

FIGURE 6. Instantaneous spatial distribution of bubbles. The graphs on the left-hand side contain data from holograms covering the region $0 < x/d < 2.2$, and a trigger transducer at $x/d = 1.25$. The graphs on the right-hand side contain data from holograms covering the region $1.6 < x/d < 3.7$ and a trigger transducer at $x/d = 2.5$. $V_j = 17.5$ m s^{-1}.

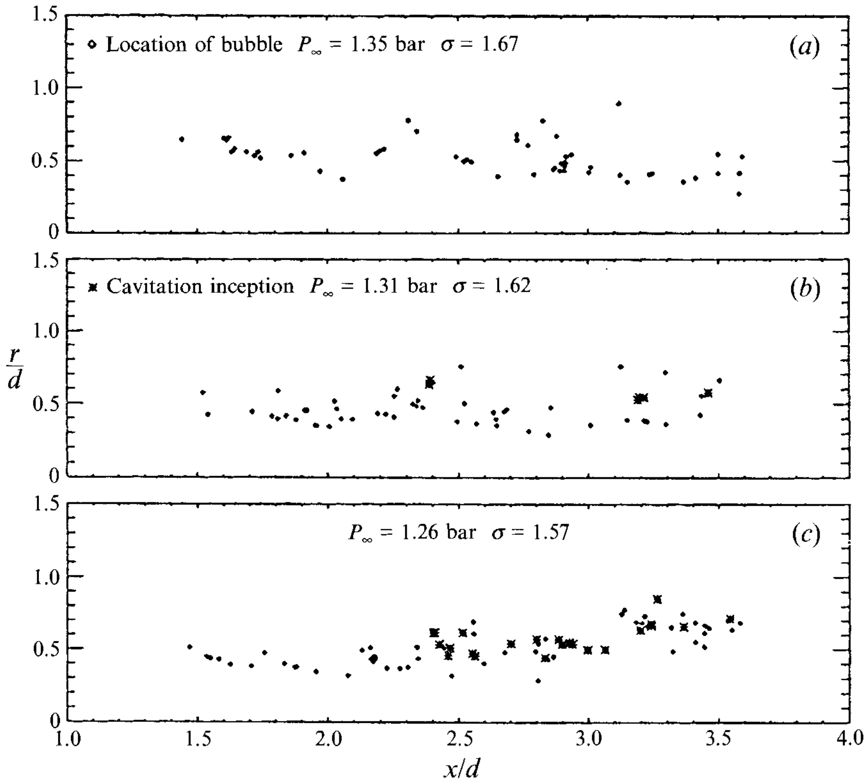

FIGURE 7. Instantaneous spatial distribution of bubbles in a 12.5 m s^{-1} jet.

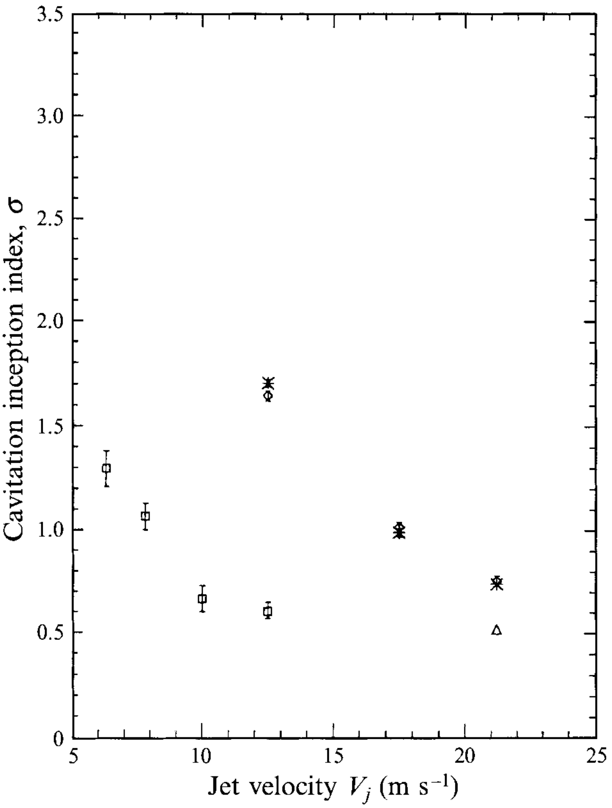

FIGURE 8. Measured inception indices of microscopic cavitation, and inception indices of macroscopic cavitation measured by Lin & Katz (1988). Present experiment: air content 28% of saturation; ◇, without roughness; *, with roughness; △, measured at $x/d = 5.2$, $r/d = 0.2$. □, Lin & Katz (1988): air content 35% of saturation, unseeded flow.

reliable lasing could occur only between 300 and 800 μs after triggering the lamp. Thus, the second ('Q switch') signal, indicating the presence of a vortex, had to occur within that time. Since the measurements were performed at jet velocities of about 18 m s^{-1}, the frequency of vortex induced pulses was 300–400 Hz (Strouhal number, fd/V_j, of 0.42–0.55). Thus, there was a typical delay of about 2.5 ms between successive pressure peaks. Consequently, the flashlamp trigger was activated about 1.5–2.0 ms after the first vortex passed by the transducer, allowing about 500 μs for the next pressure peak. When a second peak did not follow within the prescribed time, a hologram was not recorded. The 'Q switch' could be pulsed up to three times during a single flash, a feature used for measuring the velocity of the bubbles.

Another option available to us (Sridhar & Katz 1991), but not used during the present study, was to incorporate PIV (with other smaller seed particles) for simultaneous measurements of pressure and velocity. However, effective use of PIV required a high density of particles, which affected the resolution of the image of the bubbles considerably. Adopting this approach would require a separate reference beam, and modified methods for illuminating selected portions of the flow field. Future experiments will include attempts to perform such combined measurements.

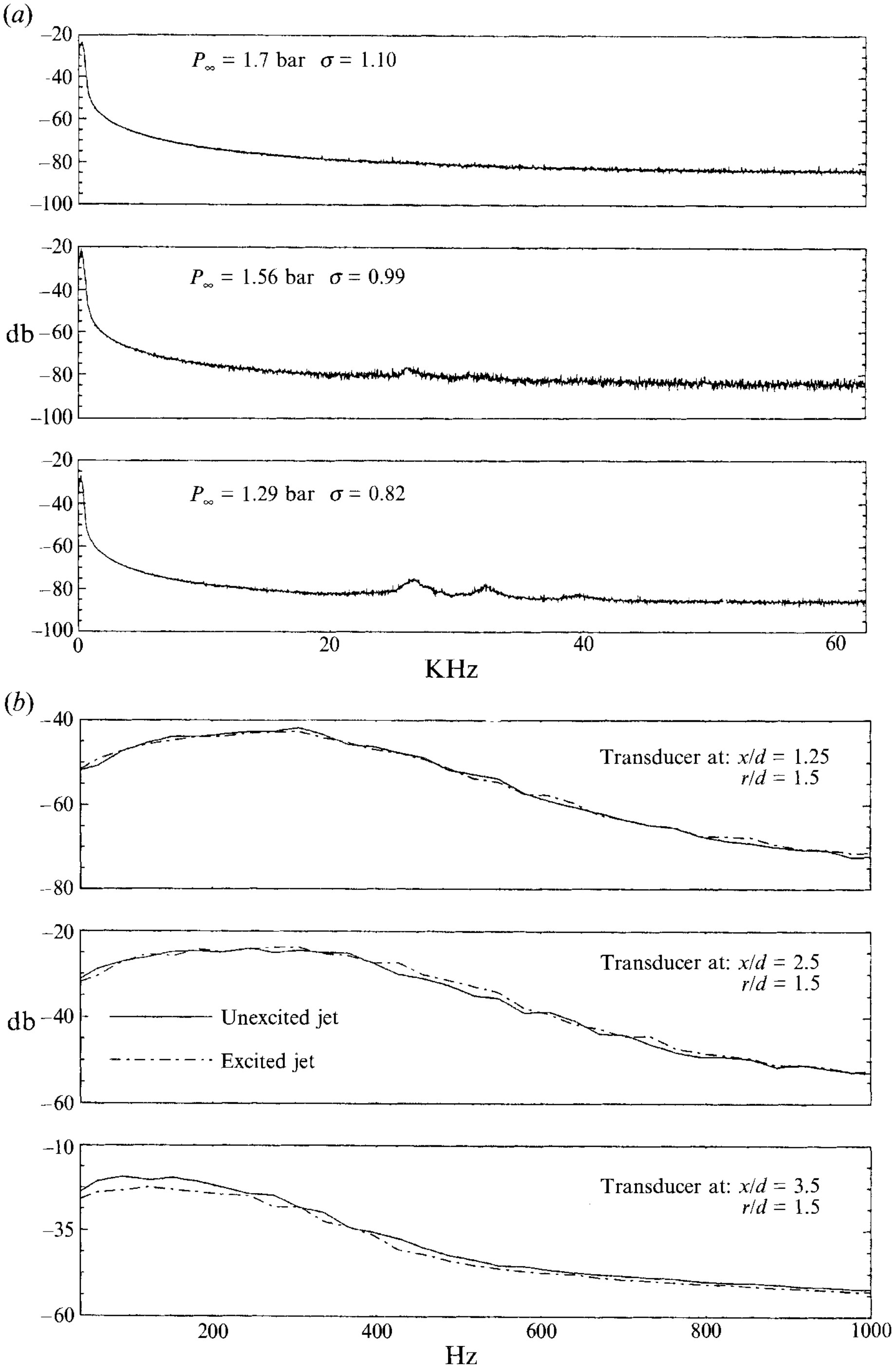

FIGURE 9. Spectra measured by the trigger transducer. (*a*) Extended frequency range. Transducer is at $x/d = 2.5$; $r/d = 1.5$, $V_j = 17.5\ \mathrm{m\ s^{-1}}$. (*b*) Low frequency range at different axial locations. $P_\infty = 1.7$ bar; $V_j = 17.5\ \mathrm{m\ s^{-1}}$; $\sigma = 1.10$.

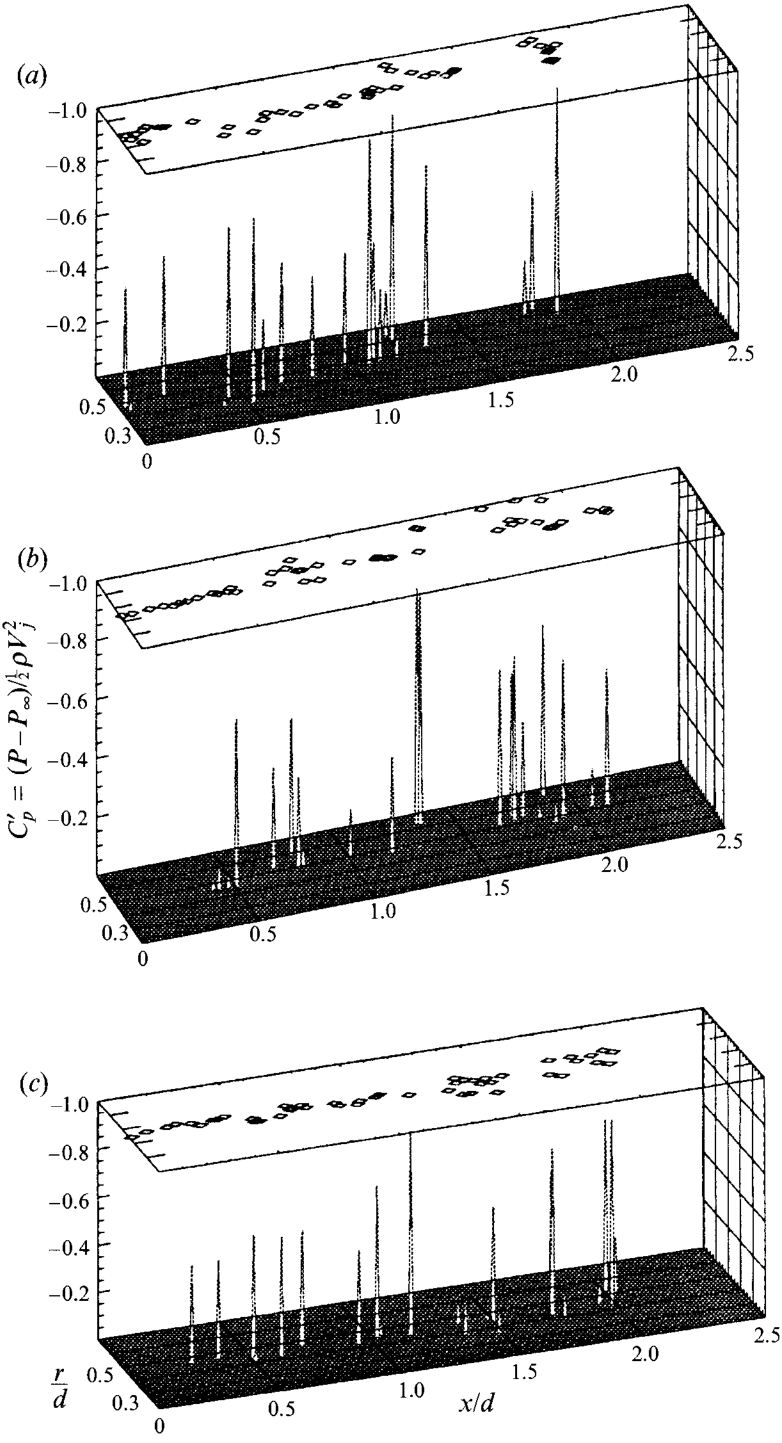

FIGURE 10(*a–c*). For caption see facing page.

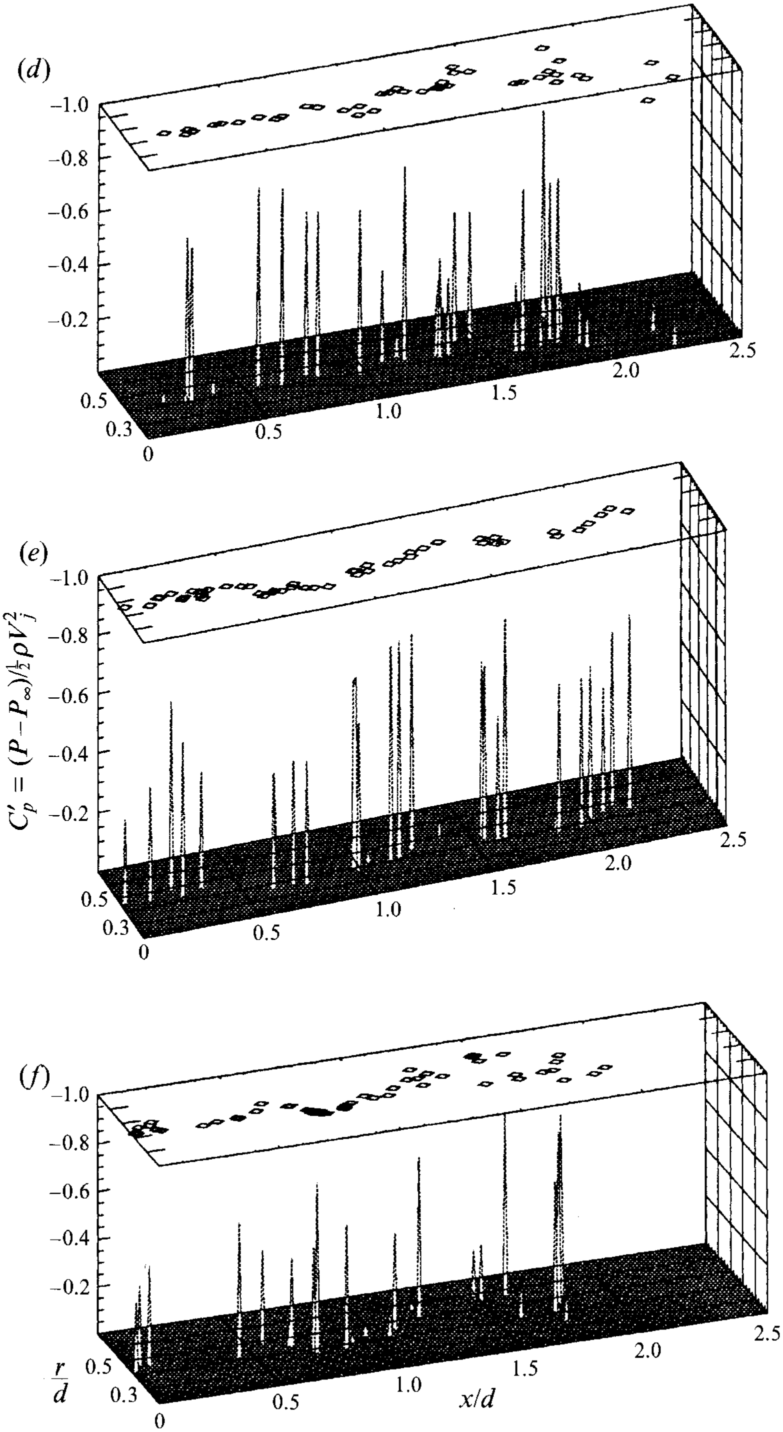

FIGURE 10. Sample instantaneous pressure distributions at $0 < x/d < 2.5$. The trigger transducer is at $x/d = 1.25$; $r/d = 1.5$. The upper plane indicates the locations of bubbles.

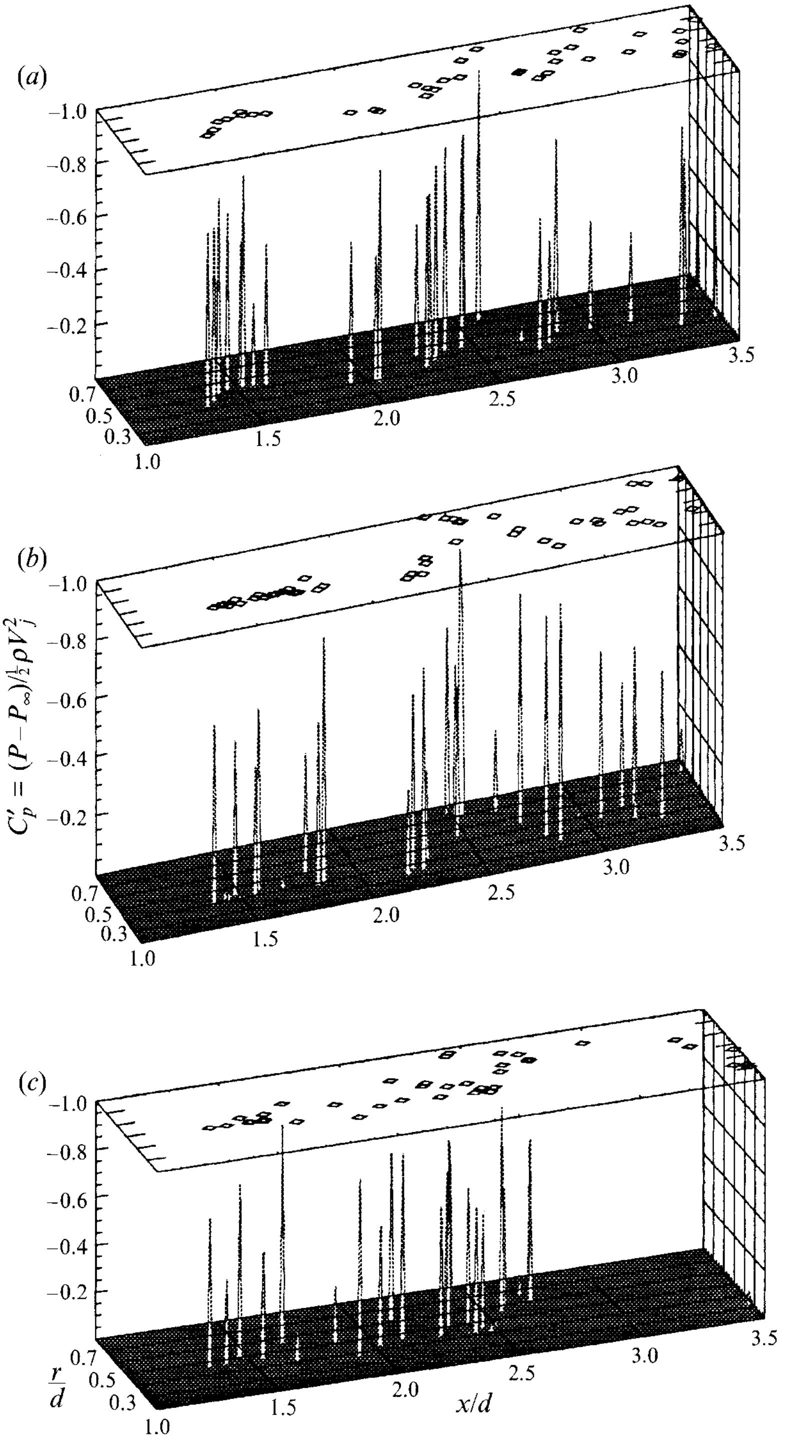

FIGURE 11(*a–c*). For caption see facing page.

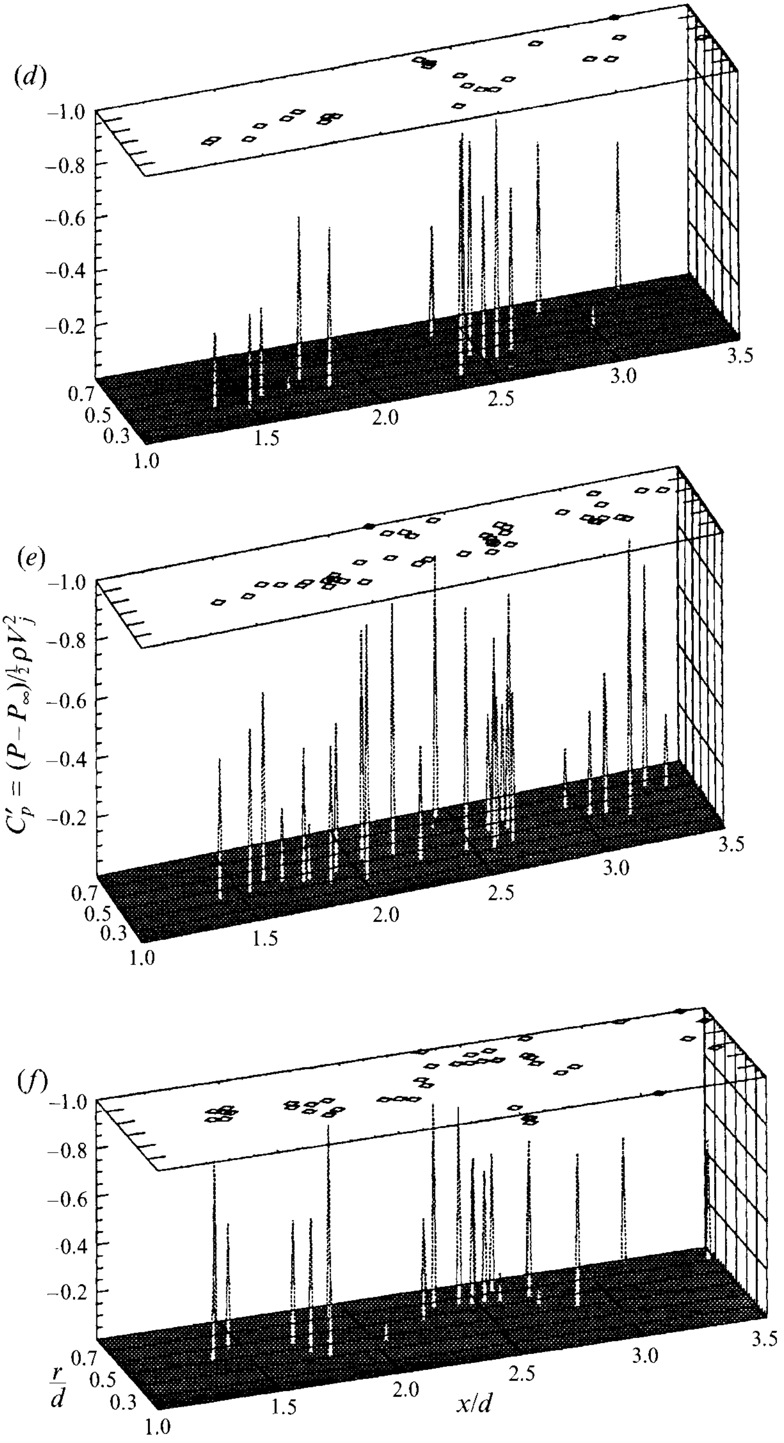

FIGURE 11. Sample instantaneous pressure distributions at $1.5 < x/d < 3.5$. The trigger transducer is at $x/d = 2.5$; $r/d = 1.5$.

3. Results: pressure fluctuations and cavitation inception

3.1. *Location and conditions for cavitation inception*

Based on earlier visual observations in the same facility by Lin & Katz (1988), it was assumed initially that cavitation inception occurred beyond the potential core, at $x/d \geqslant 5$, and that $\sigma_i \leqslant 0.4$ at velocities exceeding 20 m s^{-1}. Consequently, the experiments initially focused on this region, and measurements were performed while injecting bubbles from the centreline of the jet (some results are presented in figure 23). However, following a series of experiments involving seeding from different sites, it became evident that higher pressure fluctuations and earlier cavitation inception occurred in a different region, as illustrated in figure 5. It shows several characteristic instantaneous distributions of seed bubbles in the near field of the jet. Each sketch is composed of data obtained from several holograms since a single holograms can only cover a portion of the near field of the jet (about $\Delta x/d \approx 2.0$). Figures 5(*a*)–5(*c*) demonstrate the instantaneous location of bubbles at the same velocity (21.2 m s^{-1}) and injection point ($r/d = 0.4$), but at different ambient pressures. There are no signs of cavitation at $\sigma = 0.744$. Initially ($x/d \leqslant 2$) the bubbles appear either along a clearly defined line, or in small discrete clusters, and further downstream they start dispersing. As the cavitation index (ambient pressure) is decreased to $\sigma = 0.74$ (figure 5*b*) and then to 0.66 (figure 5*c*), there is an abrupt increase in the number of bubbles beyond $x/d = 1.9$, and odd-shaped large bubbles (such as figure 3*c*) appear in the marked sites of cavitation inception. These early signs of cavitation cannot be observed by a naked eye or detected easily by an external microphone. As will be shown later (figure 9), they are detected by the trigger transducer. When the injection point is changed to $r/d = 0$ (figure 5*d*), and as a result the near-field shear layer is not seeded, cavitation does not occur anywhere. As noted above, further reduction of pressure, to $\sigma \leqslant 0.4$, at the same velocity, causes inception of macroscopic (visible) cavitation at $x/d \geqslant 5$. Following a series of experiments involving seeding from different points, that led to distributions similar to figure 5, the focus has shifted to the near field of the jet ($x/d \leqslant 5$). These results also guided the selection of two sites for the trigger transducer. The first was located upstream of the region prone to cavitation inception, at $x/d = 1.25$ (and $r/d = 1.5$), and the second within it, at $x/d = 2.5$.

Reductions in the jet speed to 17.5 m s^{-1} and then to 12.5 m s^{-1} (figures 6 and 7), but this time using the trigger transducer, increase the cavitation inception indices to 0.99 and 1.62, respectively. Since all these flows are 'heavily' seeded with the same size bubbles, and data from numerous holograms are consistent, the values of σ_i should provide a direct indication for differences in the extent of pressure fluctuations. The reasons for this apparent strong 'Reynolds number' effect is not clear to us, but as will be shown later, it is consistent with the distributions of pressure peaks. In order to determine whether the boundary layer within the nozzle is the source of this trend, experiments were repeated also with a tripped boundary layer (created by cutting a series of 2 mm deep grooves in the nozzle). The results (figure 8), show clearly that tripping has little effect on the inception index. We do not intend to claim here that the boundary layer in the nozzle has no effect on the pressure field, since the nozzle geometry has some effect on σ_i (Lin & Katz 1988), and as Hussain & Zedan (1978) discuss, the initial conditions (momentum thickness) affect the flow structure. However, the insensitivity to roughness indicates that the significant dependence on velocity is not a result of Reynolds-number effect on the boundary layer. Note also that Kobayashi (1967), Lin & Katz (1988) and Pauchet, Retailleau & Woillez (1992) observed the same trends in the conditions for 'macroscopic cavitation' in a variety of

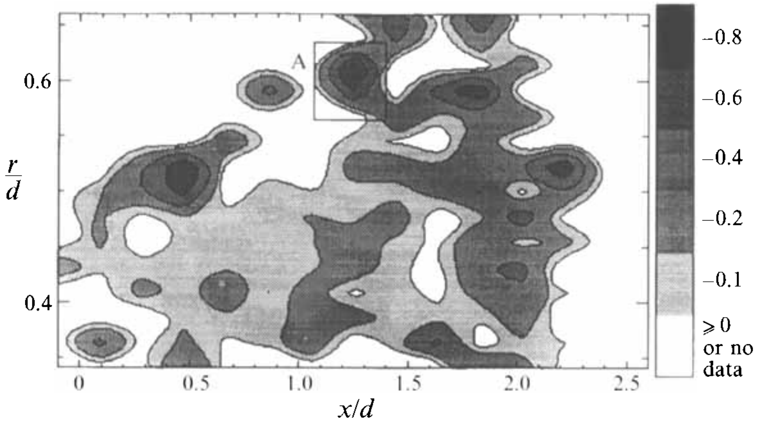

FIGURE 12. Phase averaged pressure fluctuation peaks. Trigger transducer is at $x/d = 1.25$; $r/d = 1.5$. Unexcited jet.

flow conditions. Johnson *et al.* (1982) observed the opposite trend, namely an increase in σ_i with increasing velocity.

All the distributions presented in figures 6 and 7 are obtained from holograms recorded with the trigger transducer. Consequently, each distribution with sufficiently low σ contains some cavitation sites in the vicinity of the transducer. Furthermore, there are clear signs of bubble dispersion, with or without cavitation, when the trigger is located at $x/d = 2.5$. Spectra of the transducer signal, presented in figure 9(*a*), demonstrate that during inception the signal contains clear traces of cavitation noise at 25 KHz, that increase in energy as the pressure decreases. By focusing on the hydrodynamic (low frequency) portion of the spectrum, as shown in figure 9(*b*), it is also evident that the peak frequency decreases by about a half, from 300 Hz to 150 Hz between $x/d = 1.5$ and 3.5. Thus, vortex pairing occurs somewhere between these points. At $x/d = 2.5$, the peak is shifted slightly towards lower frequencies (compared to $x/d = 1.5$), suggesting that pairing starts in this region. Thus, it seems that dispersion of bubbles, and the onset of cavitation occur close to the site of vortex pairing. This conclusion will become more evident from the results of pressure measurements. Another issue associated with figure 9(*b*), namely the small difference between spectra of the excited and unexcited jets will be discussed in §3.3.

3.2. *Pressure distributions in an unexcited jet*

Sample instantaneous pressure distributions within an unexcited jet, as measured by using the bubbles, are presented in figures 10 and 11. Each distribution contains 30–50 data points determined from all the bubbles in a single hologram. The magnitudes of negative peaks and the locations of all the bubbles are shown in each plot. Only a few samples are presented in order to demonstrate the extent of variability in the spatial distributions of available data. The first series (figure 10) contains data obtained from holograms recorded with a trigger transducer located at $x/d = 1.25$, and as a result one can almost always identify at least one high negative pressure peak in the vicinity of the transducer. The peaks and bubble clusters tend to appear in discrete locations, such as $x/d = 0.5$, 1.25 and 1.9 in figure 10(*a*), which is a representative of the most commonly observed trend. Assuming that these peaks represent the sites of the primary shear-layer eddies, then the wavelength, λ, in the near field is about $0.7d$. There are, however, considerable differences between the instantaneous distributions. The

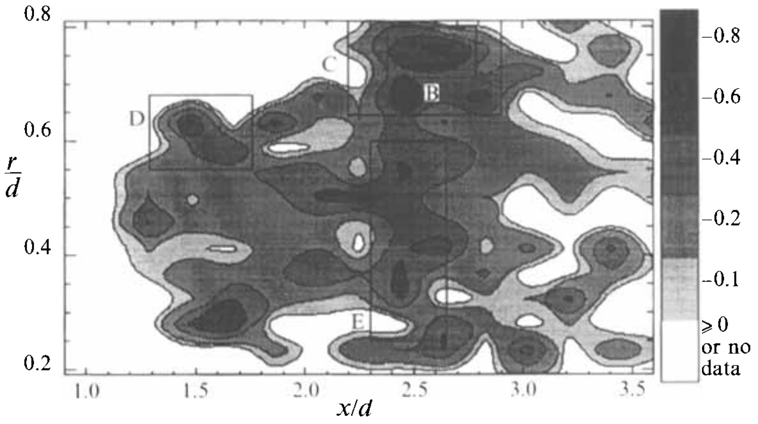

FIGURE 13. Phase averaged pressure fluctuation peaks. Trigger transducer is at $x/d = 2.5$; $r/d = 1.5$.

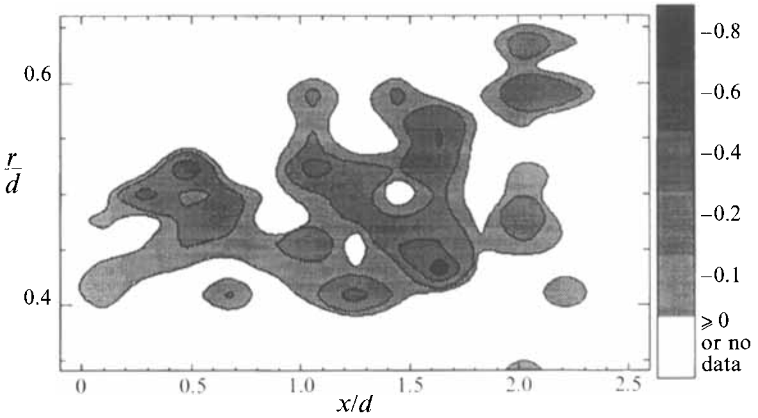

FIGURE 14. Phase averaged pressure fluctuation peaks. Trigger transducer is at $x/d = 1.25$; $r/d = 1.5$, but the trigger signal is delayed by 1000 μs.

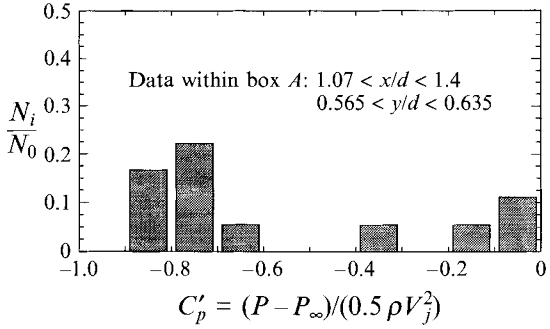

FIGURE 15. Probability histogram of pressure fluctuation peaks within an area centred around $x/d = 1.25$; $r/d = 0.6$, and bounded by the box A shown in figure 12. $P_\infty = 1.7$ bar; $V_j = 17.5$ m s^{-1}. N_i = number of pressure peaks with the indicated amplitude; N_0 = total number of pressure peaks.

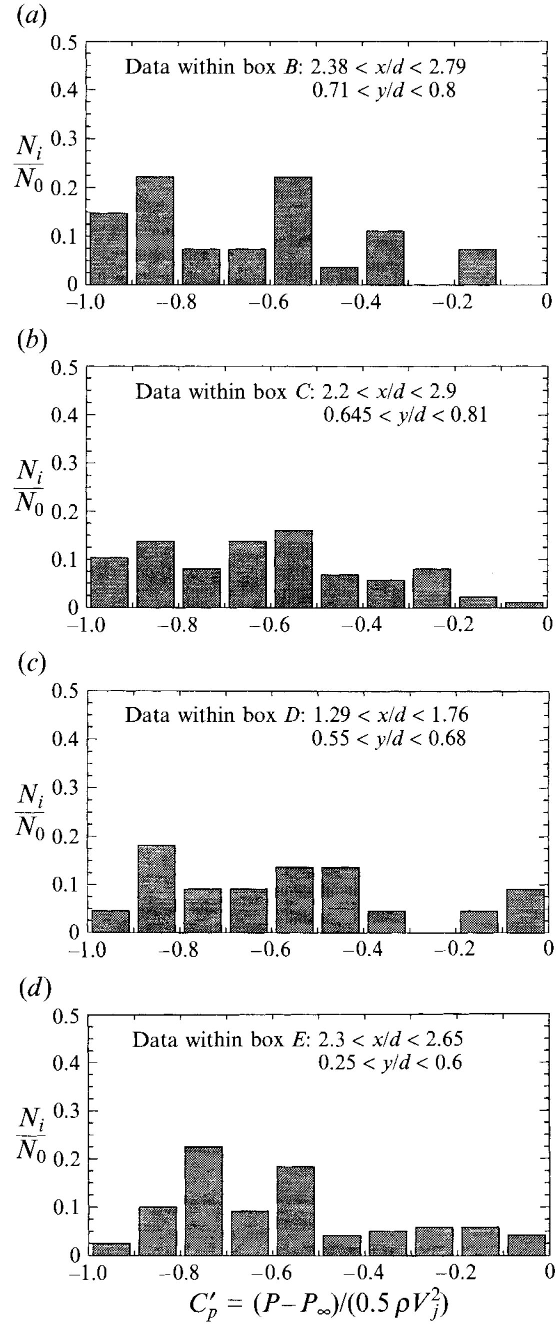

FIGURE 16. Probability histograms of pressure fluctuation peaks within the region: (*a*) bounded by box B in figure 13; (*b*) bounded by box C; (*c*) bounded by box D; (*d*) bounded by box E. P_∞ = 1.7 bar; $V_j = 17.5\ \mathrm{m\ s^{-1}}$.

location of minimum pressure is not necessarily the site of bubble clusters (figure 10*b, c*), and in some cases the minimum pressure peaks seem to be randomly distributed (figure 10*d, e*). Dispersion of bubbles, apparently due to the onset of the vortex pairing process, starts typically at $x/d \approx 1.5$ (figure 10*f*), but the exact location

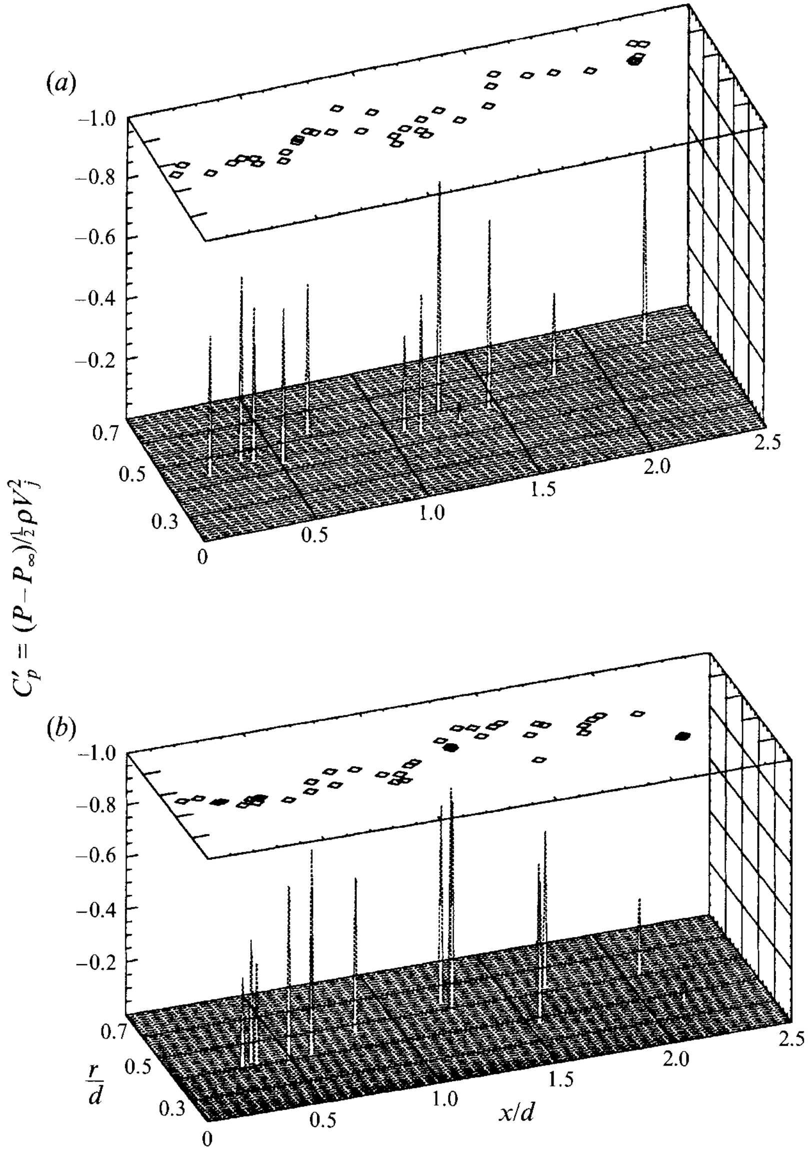

FIGURE 17(a,b). For caption see facing page.

fluctuates considerably. The second series of instantaneous distributions (figure 11) consists of data recorded when the transducer is located at $x/d = 2.5$. Here the bubbles are already scattered over an area extending between $r/d = 0.3$ and 1.0. Discrete clusters with high pressure peaks are clearly evident (figure 11a, b), but there is a considerable variability in the magnitude and location of pressure peaks (figure 11c–f).

The 'phase averaged' pressure distributions were determined by dividing the flow field into sections, with sizes $\Delta x/d = 0.164$ and $\Delta r/d = 0.04$, and averaging all the available data in each section (with the transducer at the same location). Results are presented in figures 12 and 13. As expected, the presence of negative pressure peaks at the sites of the trigger transducer ($x/d = 1.25$ and 2.5, respectively) are clearly evident. For comparison, and in order to add confidence that this phase averaging is not an 'art

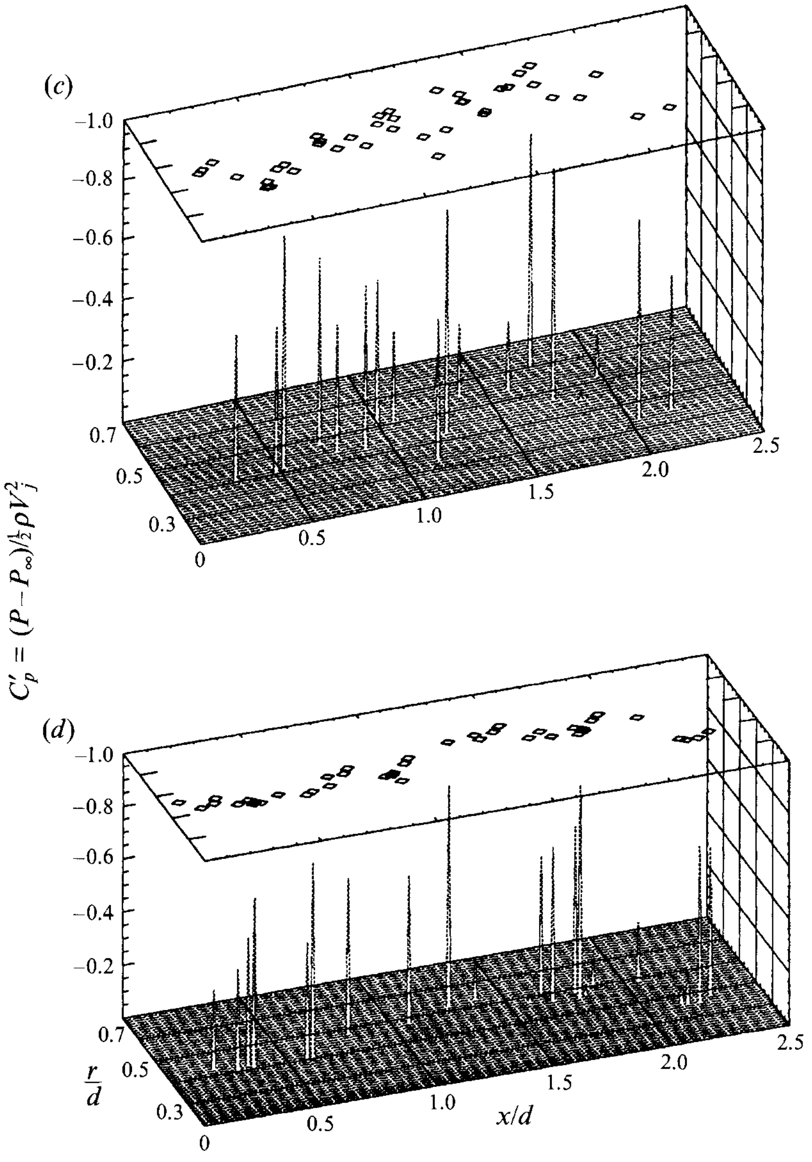

FIGURE 17. Sample instantaneous pressure distributions at $0 < x/d < 2.5$, with external acoustic excitation.

effect', figure 14 contains data recorded 1 ms ($tV_j/d = 0.69$) after the transducer located at $x/d = 1.25$ senses the negative pressure peak. The differences between figures 12 and 14 are obvious. Note that the distributions contain additional peaks. In figure 12 there is a peak at $x/d = 0.5$, in agreement with the instantaneous data shown in figure 10(*a*), and figure 13 contains a region of high fluctuations between $x/d = 1.5$ and 2.0. In fact, with a little imagination the latter distribution shows a stage in the process of vortex pairing.

Probability histograms showing the distribution of results within the region surrounding the peak, and marked as *A* in figure 12, are presented in figure 15. About 66% of the peaks are negative, 44% are below -0.6, and 39% are below -0.7. Considering that region *A* is larger than the vortex core (it covers $\Delta x/d = 0.33$ and

$\Delta r/d = 0.07$), and as a result not all the bubbles are located near the minimum pressure point, this histogram indicates that the chosen 'conditional sampling' method is successful. In this region the magnitude of the pressure peaks are clearly lower than the inception index at this velocity. However, as figure 6 indicates, reduction in ambient pressure to $\sigma < 0.9$ results in cavitation inception at $x/d < 1.5$, in complete agreement with the results of pressure measurements.

Histograms of pressure peaks in selected regions when the trigger is located at $x/d = 2.5$, and are marked as *B–E* in figure 13, are presented in figure 16. In section *B* (figure 16*a*), which includes the main low-pressure region, 15% of the negative peaks fall within the -0.9 to -1.0 range, in agreement with the values of σ_i. In fact, the highest pressure peaks, -0.97, are almost a perfect match (within the present accuracy) with the cavitation inception indices (0.99 according to figure 6), namely:

$$\sigma_i + C'_P = \frac{P_{\infty i} - P_v}{\frac{1}{2}\rho V_j^2} + \frac{P - P_{\infty i}}{\frac{1}{2}\rho V_j^2} = \frac{P - P_v}{\frac{1}{2}\rho V_j^2} = 0.02 \approx 0. \tag{11}$$

Although one would expect to obtain such results when 'weak' cavitation nuclei ('weakness' is defined by the magnitude of tension required for inception, as evaluated by (1)) are readily available, such a correspondence has never been proved in turbulent shear flows, owing to lack of experimental data.

Extending the area, over which the data is averaged, to section *C* (figure 16*b*) only adds smaller peaks, with values above -0.8, to the distribution of section *B*. Thus, the high negative pressure peaks are confined to a small region, presumably the vortex core. Near the second site of low phase averaged pressure, which is located around $x/d \approx 1.5$ and $r/d \approx 0.55$ and identified as section *D*, only 4% of the peaks are lower than -0.9 (figure 16*c*), and a total of 20% are below -0.8. Thus, one should expect that this region is less prone to cavitation inception. Finally, within the area identified as section *E* (figure 16*d*), which is located at about the same x/d as the primary vortex, but closer to the centreline of the jet, only one out of 72 data points has a value below -0.9. The bulk of the data falls between -0.5 and -0.8. Similar distributions can be obtained for other sections of the near field of the jet, provided they are seeded with bubbles. They will be used later for estimating the probability of cavitation inception.

3.3. *Effect of acoustic excitation*

Much has been written already on the effect of acoustic excitation on the flow structure of turbulent jets (see an extensive summary by Hussain 1986, as well as detailed experiments by Zaman & Hussain 1980; and Hussain & Zaman 1980, 1981), and a complete study of this issue is beyond the scope of the present paper. However, it is interesting to examine whether excitation has a significant effect on the pressure field and conditions for cavitation inception. The so called 'preferred mode' was selected based on the spectrum of the trigger transducer of an unexcited jet at $x/d = 1.25$, which according to figure 9(*b*) had a peak Strouhal number of about 0.5. As described before, the flow was excited using a speaker as the initial source and adjusting the length of the pipe upstream of the nozzle to amplify its signal. This method had a fairly small effect on the spectrum of the trigger transducer, as shown in figure 9(*b*), and thus it should be categorized as 'weak excitation' (additional discussion follows). However, it had a considerable effect on the pressure field.

Sample, typical, instantaneous pressure distributions of an excited jet, when the trigger is located at $x/d = 1.25$, are presented in figure 17. The corresponding phase averaged results, and probability histogram of data in the vicinity of the main peak, are

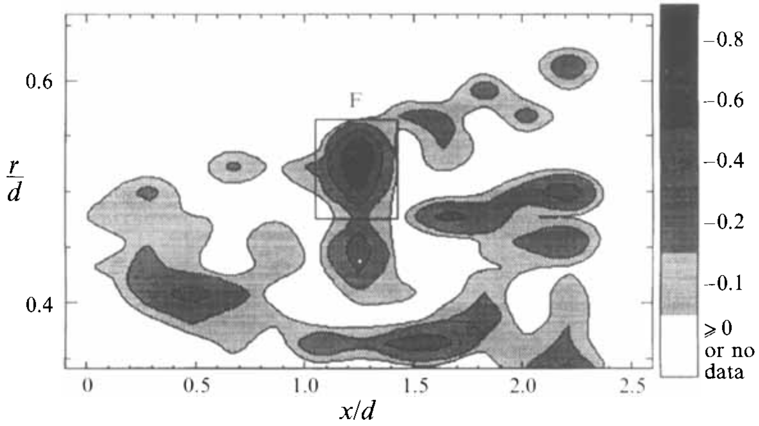

FIGURE 18. Phase averaged pressure fluctuation peaks with external acoustic excitation. Trigger transducer is at $x/d = 1.25$; $r/d = 1.5$.

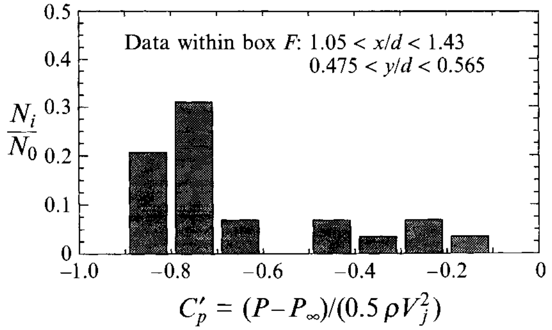

FIGURE 19. Probability histogram of pressure fluctuation peaks within the area bounded by box F in figure 18. $P_\infty = 1.7$ bar; $V_j = 17.5 \text{ m s}^{-1}$.

presented in figures 18 and 19, respectively. From the latter it is clear that phase averaging is equally successful in the excited jet (compare to figure 15), and that about 50% of the peaks are in the -0.7 to -0.9 range. By comparing figures 18 and 14, it is evident that acoustic excitation alters the flow structure. It shifts the location of the minimum pressure point (presumably the vortex core) from $r/d = 0.63$ to $r/d = 0.5$, and reduces the number and magnitude of other peaks. In fact, unlike the results of an unexcited jet, figure 18 does not contain any other point with phase averaged pressure below -0.6. However, the variability in the instantaneous distributions still exists, and local minima can still be identified at $x/d = 0.5$ and 1.9 (see also figure 17*a*, *c*). Thus, the type of excitation used in the present study reduces the number and energy of these structures, but does not eliminate them.

Excitation also affects the pressure further downstream, as demonstrated by a few samples of instantaneous distributions, and phase averaged map, shown in figures 20 and 21, respectively. In the typical distributions (figure 20*a*, *b*) vortex pairing is not evident, and the primary pressure peaks are located much closer to the centreline, at $r/d = 0.45$, compared to 0.77 in an unexcited jet. In fact, in most holograms of an excited jet the bubbles are concentrated within $r/d < 0.6$. In rare cases (figure 20*c*) there are traces of pairing, and some instantaneous distributions (figure 20*d*), typically

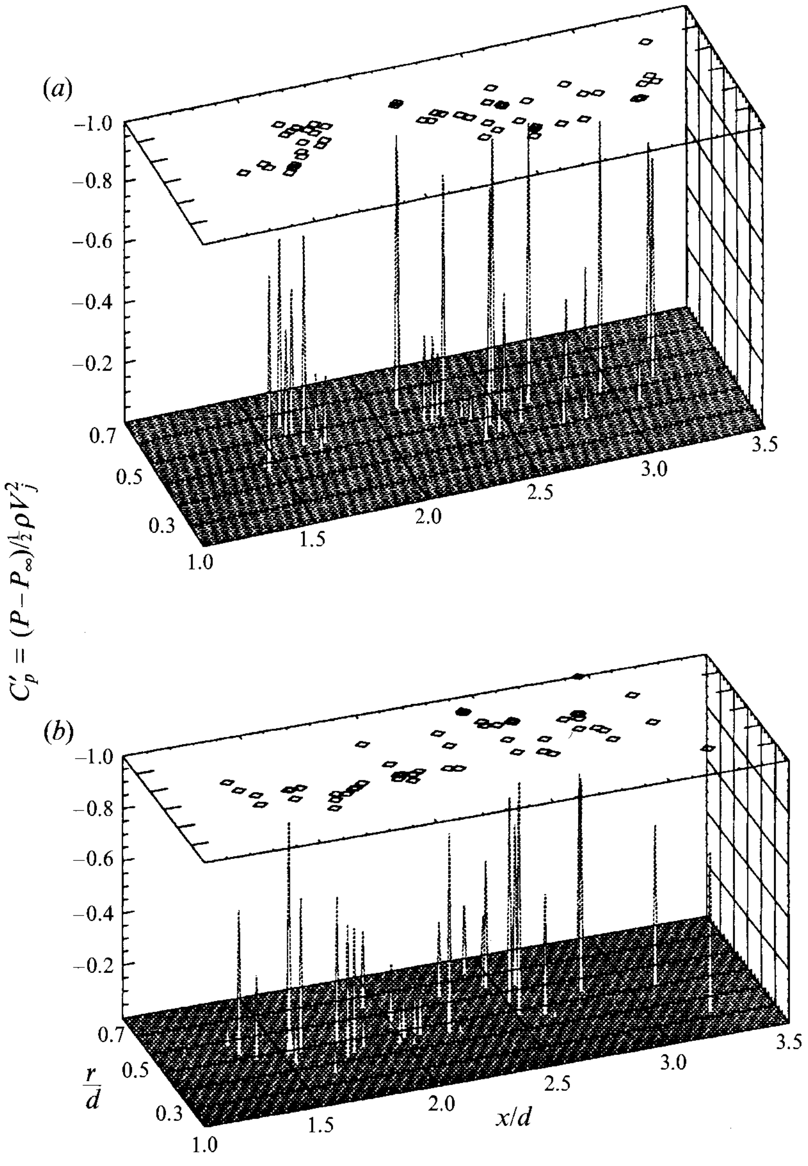

FIGURE 20(*a*, *b*). For caption see facing page.

about 20% of them, contain dispersed bubbles, without any clear evidence of a preferred spatial distribution. Suppression, or at least modification of the pairing process, owing to acoustic excitation at the preferred modes of the shear layer, has been reported before (see Ho & Huerre 1984 for a detailed summary). The present measurements confirm this phenomenon, and demonstrate its impact on the pressure field.

Probability histogram of pressure peaks near the minimum pressure point is presented in figure 22. Unlike the unexcited flow, which is dominated by vortex pairing, the peaks of the excited jet are scattered everywhere. In section *G* only 5% of the peaks are higher than -0.9. However, additional peaks of similar magnitudes exist in different sites, particularly when the bubbles appear dispersed (figure 20*d*). The overall

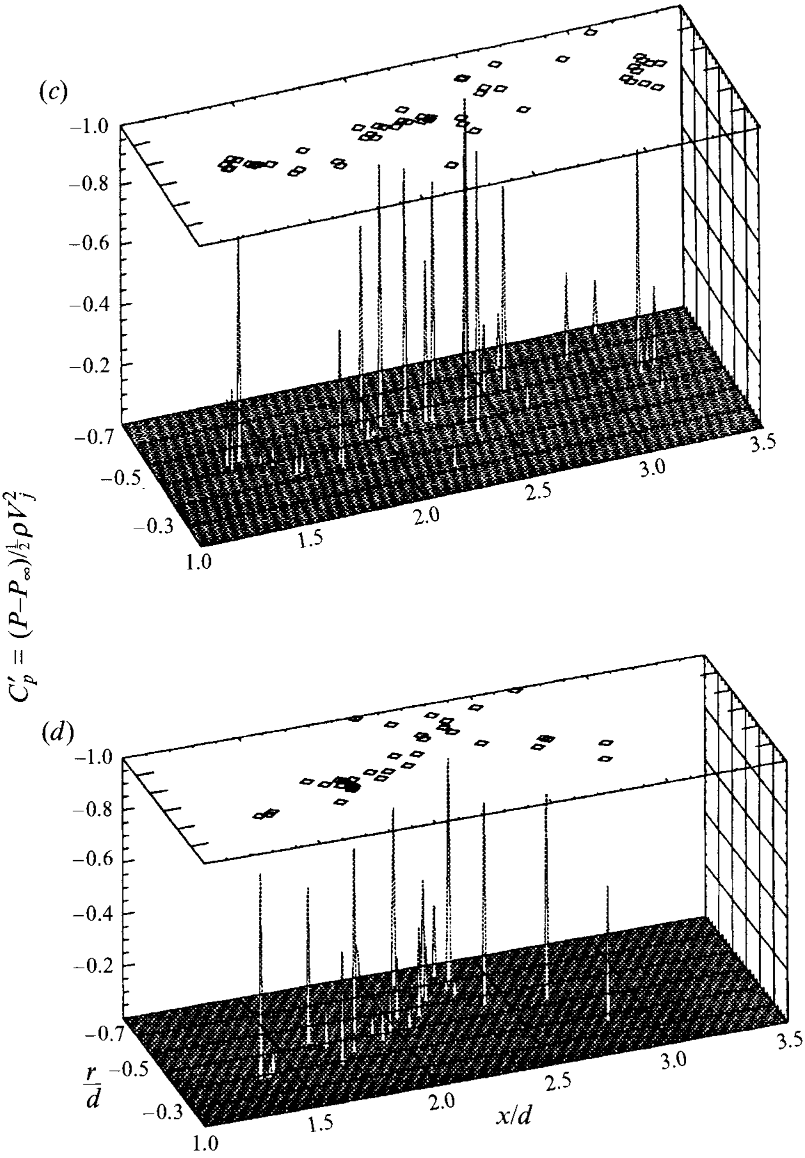

FIGURE 20. Sample instantaneous pressure distributions at $1.5 < x/d < 3.5$ with external excitation.

percentage of peaks reaching below -0.9 is only slightly lower than the unexcited jet. Thus, one should not expect to see a major impact on the conditions for cavitation inception. In fact, early traces of cavitation appears within the excited jet at the same inception index, $\sigma_i = 0.99$, and the trigger transducer signal has the same spectral peak above 25 KHz (data not shown, the effect of cavitation appears to be almost identical to figure 9*a*). It is difficult to compare the number of cavitation events, since the collapsing bubbles appear at different locations. However, if one filters the transducer signal with a high-pass filter, at a cutoff frequency of 15 KHz, the number of high pressure peaks should be a qualitative indicator for the number of cavitation events. Performing such an analysis (data not shown) does not lead to any conclusive answers at any cavitation index, below and above the inception level. At $\sigma = 0.99$, for example,

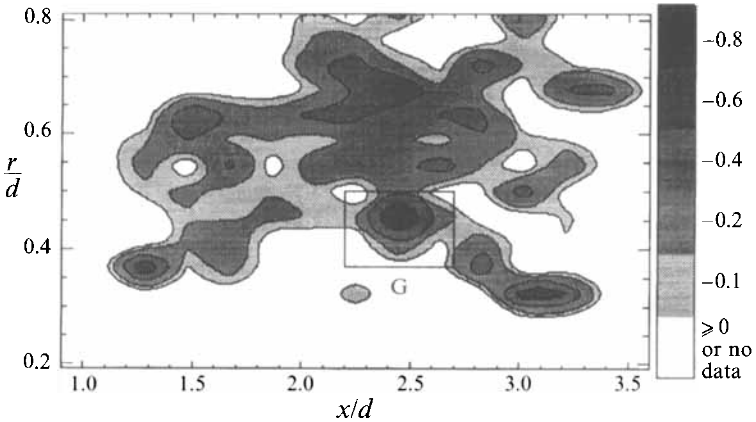

FIGURE 21. Phase averaged pressure fluctuation peaks with external acoustic excitation. Trigger transducer at $x/d = 2.5$; $r/d = 1.5$.

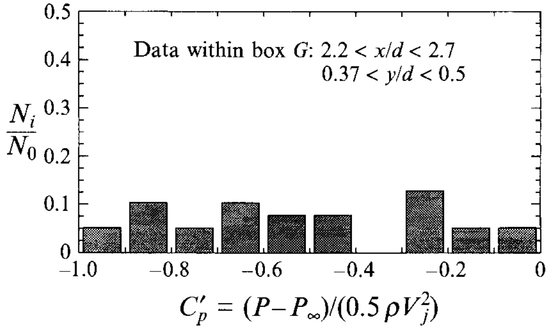

FIGURE 22. Probability histogram of pressure fluctuation peaks within the area bounded by box G in figure 21. $P_\infty = 1.7$ bar; $V_j = 17.5$ m s^{-1}.

the number of peaks of an excited jet is lower by a few per cent. Thus, one has to conclude that although acoustic excitation (of the kind used in the present study), alters the flow structure, the effect of the inception index and rate of cavitation events is small. This conclusion should not be generalized to any form of forced jets, particularly not to cases of strong excitation. In another study, involving enhancement of cavitation using specially designed, 'self excited' nozzles, Johnson *et al.* (1982) show that sufficiently strong excitation can increase the inception indices (presumably of macroscopic cavitation – since they can see the cavities).

Another unresolved issue is the little effect acoustic excitation has on the hydrodynamic spectra of the trigger transducer (figure 9*b*). To explain this puzzling result, recall that this transducer is located outside the jet and detects only the motion of large-scale structures. Thus, its output should have little resemblance to the spectra of pressure fluctuations within the jet. Furthermore, since the excitation frequency is based on the signal of an unexcited jet, one should at most expect some narrowing of the spectral peaks at $x/d = 1.25$. Being weak excitation, it apparently has little effect on the trigger signal. There are two subtle differences between the spectra in figure 9(*b*). The first is a slight shift in the location of the peak at $x/d = 2.5$, which is consistent with the delay in pairing process. Secondly, there is a small, but consistent difference in energy level (by about 3 db) at $x/d = 3.5$. The latter may be caused by a larger

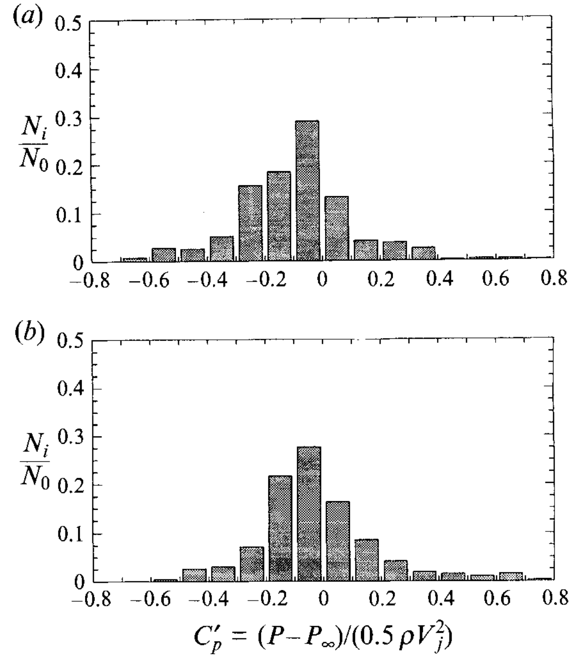

FIGURE 23. Probability histograms of pressure fluctuation peaks at $4 < x/d < 6.5$ and $0 < r/d < 0.65$. (*a*) $V_j = 17.5$ m s^{-1}; $P_\infty = 1.75$ bar. (*b*) $V_j = 21.2$ m s^{-1}; $P_\infty = 1.67$ bar. N_i = number of pressure peaks with amplitude of C_p'. N_0 = total number of pressure peaks.

distance between the vortices and the transducer, also in agreement with the present measurements.

3.4. *Pressure fluctuations beyond the potential core*

The puzzling dependence of σ_i on velocity (figure 8), requires a comparison between the distributions of pressure peaks. We chose to focus on the region of macroscopic cavitation inception, namely just beyond the end of the potential core ($4.0 < x/d < 6.5$, and $0.0 < r/d < 0.65$). We did not attempt to use conditional sampling in this region, owing to the 'random' nature of the transducer signal, and as a result we do not present the spatial distribution. Probability histograms of pressure peaks for this region, each computed from at least 600 data points, are presented in figure 23. Both distributions are skewed, and the computed r.m.s. values (0.24 and 0.26 for 17.5 and 21.2 m s^{-1}, respectively) are very close. However, when one focuses on the high negative pressure peaks, there is a considerable difference between these distributions. At 17.5 m s^{-1} 3.6 % of the peaks are below -0.5, compared to only 0.7 % at 21.2 m s^{-1}. Thus, trends in the distribution of negative pressure peaks are consistent with the measured cavitation inception indices (figure 8). The impact of these results on the probability of cavitation inception will be discussed later. Note also that the r.m.s. values do not provide even a clue on the distributions of high pressure peaks. As a result, attempts to explain trends in cavitation inception, as was done in the past, with Reynolds averaged flow properties (either velocity or pressure fluctuations) have very little chance of succeeding. One can even speculate on the reasons for this phenomenon, such as the effect of the local velocity on the dissipation (or cascading) of energy of the large eddies. However, such a discussion is beyond the scope of the present paper.

3.5. *Discussion*

To the best of our knowledge, there is no other source containing information on the distribution of pressure fluctuation peaks within the near field of a jet. Consequently, we cannot compare the present results to any other measurement. Root mean square values (e.g. Barefoot 1972) are usually at least an order of magnitude smaller, and as a result do not help in explaining or predicting the conditions for cavitation inception. Efforts to predict the pressure spectra, using Kolmogorov similarity rules (see discussion by George *et al.* 1984 as well as Arndt & George 1978), are usually successful in idealized flows (homogeneous turbulence or simple shear), or in scales which are considerably smaller than the size of the coherent structures. As the present study clearly demonstrates, the high-pressure fluctuations within the near field of the jet are related directly to the dynamics of coherent structures (at least in the present range of Reynolds numbers). Specifically, it seems that the highest negative pressure peaks, and the onset of cavitation occur during vortex pairing. Although development of an acceptable model, that predicts these high peaks, would be presumptuous, simple scaling can at least show that the present results are reasonable.

The circulation of a single vortex primary can be estimated crudely as $V_j \lambda$, where λ is the characteristic wavelength (distance between structures). Assuming a uniformly distributed vorticity within a vortex core having a radius, r_c (solid body rotation), and ignoring the role of secondary vortices (a discussion follows) the pressure in the centre of this vortex is:

$$C_{Pc} = \frac{P_c - P_\infty}{\frac{1}{2}\rho V_j^2} \approx -\frac{1}{\pi^2}\left(\frac{\lambda}{r_c}\right)^2. \tag{12}$$

The ratio λ/r_c should have a value varying between 2 and 4, and as a result C_{Pc} must fall between 0.4 and 1.6. Thus, the measured levels of negative pressure peaks are reasonable (a ratio of 2.8 provides the proper answer). During the early stages of pairing the radius of one of the vortex rings increases (from $r/d = 0.62$ to 0.77 in an unexcited jet), resulting in vortex stretching, and a reduction in r_c. Assuming that the volume of the vortex remains unchanged, namely $r_c^2 r_v$ is constant (r_v is the radius of the ring), then $-C_{Pc}$ is proportional to r_v. Consequently, it is reasonable to expect that $-C_{Pc}$ increases from a typical value of 0.78 to about 0.97 as a result of the stretching. This simplified approach can explain why the region of vortex pairing is the most likely site for cavitation inception. Note that this type of axisymmetric stretching does not occur in a two-dimensional shear layer, where the vortex is simply displaced.

As noted before, an important component ignored in this discussion is the role of secondary structures, or braids, in the onset of cavitation. As observed by Katz & O'Hern (1986) and investigated in detail later by O'Hern (1987), these braids are the primary sites of cavitation inception in a large-scale two-dimensional shear layer developing behind a sharp-edged plate (Reynolds numbers $> 10^6$). Furthermore, cavitation appears first in portions of the braids, which are located between the primary vortices. O'Hern also made some pressure measurements with microscopic bubbles, but provided only a single probability distribution determined from a total of 65 measurements, without spatial distribution or phase averaging. Using Ran & Katz (1991) calibrations, he measured negative pressure peaks in the order of -2.0, matching his cavitation inception indices in saturated water. Thus, there is an apparent disagreement between the present argument, that inception occurs in the core of the primary structures, and Katz & O'Hern's (1986) results. Note that Lin & Katz (1988) demonstrate that these braids exist in the jet, and that cavitation extends into them, but only at a much lower σ. We do not have a well-founded explanation for this discrepancy at the present time, besides noting the obvious, namely that the shear-layer experiments were performed at Reynolds numbers away above 10^6. However, by careful examination of the two experiments, as well as some of the references associated with figure 1, possible reasons for the disagreement can be identified.

From Katz & O'Hern's and O'Hern's photographs, it is evident that early traces of macroscopic cavitation appear in the braids only after several generations of vortex pairing (at least three according to O'Hern), typically at $Re_x > 6 \times 10^6$ (Re_x is the Reynolds number based on the axial distance from the origin). Closer to the separation point cavitation occurs only at lower σ, and when it does occur, it appears predominantly in the primary vortices. These observations suggest that several cycles of pairing are needed in a plane shear layer before the secondary structures have enough circulation to become the primary sites of inception. We obviously do not know if one can generalize this conclusion and it is not within the scope of the present work. The implication of this suggestion for jet cavitation is discussed below.

The flow in the near field of a jet resembles a shear layer only until the end of the potential core ($x \sim 5d$). An estimate for the number of pairing processes that can occur in this region is the ratio of the wavelength at the end of the potential core, λ_c (column mode, as defined by Hussain 1986), to the wavelength during initial vortex roll-up, λ_s (shear-layer mode). λ_c can be estimated as the convection velocity ($\sim 0.5 V_j$) divided by the frequency ($= St_c V_j/d$, where St_c is the column mode Strouhal number, whose values vary between 0.25 and 0.5). Thus, $\lambda_c \propto d/St_c$. λ_s is proportional to the momentum thickness, θ, of the boundary layer at separation (Ho & Huerre 1984), which depends on the flow within the nozzle. Thus, the number of pairing processes is dependent on the ratio d/θ. Typical values of d/θ range between 100 and 300, and the number of pairing processes in a jet ranges between 2 and 3. This relationship offers a possible mechanism for size effects on the inception index, that is clearly evident from figure 1. If the jet diameter is increased, without changing θ (depending on the experimental set-up d and θ may be related), the number of possible pairing processes also increases, and as a result the strength of the secondary vortices (if our assumption about the relationship between pairing and strength of braids is correct). Note that small changes in either diameter or momentum thickness may be insufficient to cause an additional pairing. Thus, increasing the velocity, for example, that for a laminar boundary layer in the same nozzle, should cause a reduction in θ ($\theta/x \propto 1/(Re_x)^{0.5}$), may have no effect on the number of pairing processes. If the boundary layer is turbulent, as is probably the case for most of the data included in figure 1 (it is not clearly stated, but judged from the experimental set-up), θ is weakly dependent on the Reynolds number, and an increase in jet diameter should cause an increase in the number of pairing processes. This conjecture is a possible mechanism in which the jet diameter has a direct impact on the conditions for cavitation inception. One should also keep in mind that an increase in V_j (Reynolds number) may cause earlier breakdown of coherent structures to smaller scale turbulence, which would reduce the pressure peaks in the vortex core. Thus, it is possible that increasing the jet velocity would cause a decrease in σ_i, as we have seen in the present study.

Indirect (and speculative) support for this argument can be inferred from Kobayashi's (1967) measurements of inception indices in standard, industrial, smooth nozzles. His results suggest that the values of σ_i increase in 'steps' as the nozzle diameter is increased. For example, σ_i increases when the diameter increases from 57 to 80 and to 114 mm, and then remains unchanged when the diameter is further increased to 135 mm. Depending on velocity, further increase to 160 mm causes again

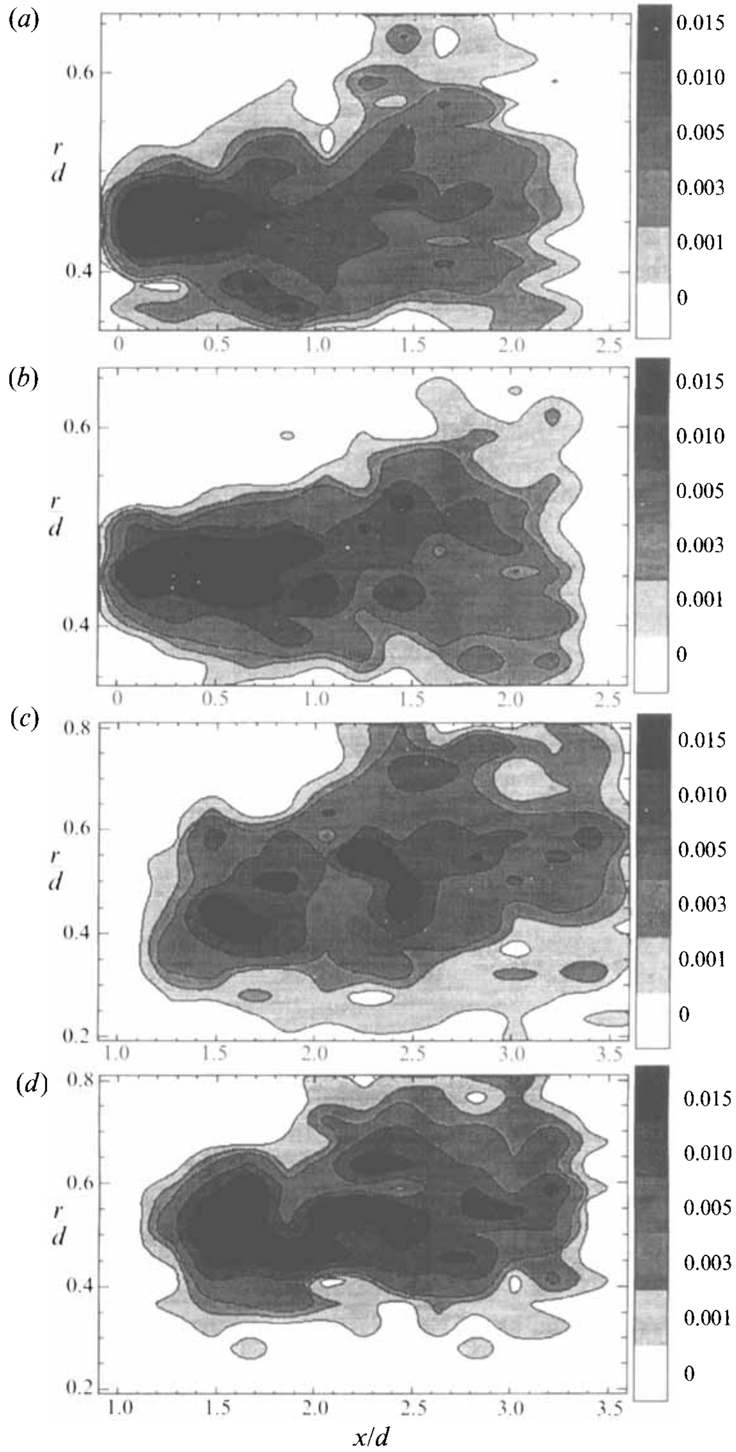

FIGURE 24. Phase averaged spatial distributions of bubble. The plots indicate the number of bubbles, N, within an area of $\Delta x/d = 0.164$; $\Delta r/d = 0.04$, divided by the total number of bubbles, No. (*a*) The trigger is at $x/d = 1.25$; $r/d = 1.5$; without excitation; No = 925. (*b*) The trigger is at $x/d = 1.25$; $r/d = 1.5$; with excitation; No = 907. (*c*) The trigger is at $x/d = 2.5$; $r/d = 1.5$; without excitation; No = 867. (*d*) The trigger is at $x/d = 2.5$; $r/d = 1.5$; with excitation; No = 655.

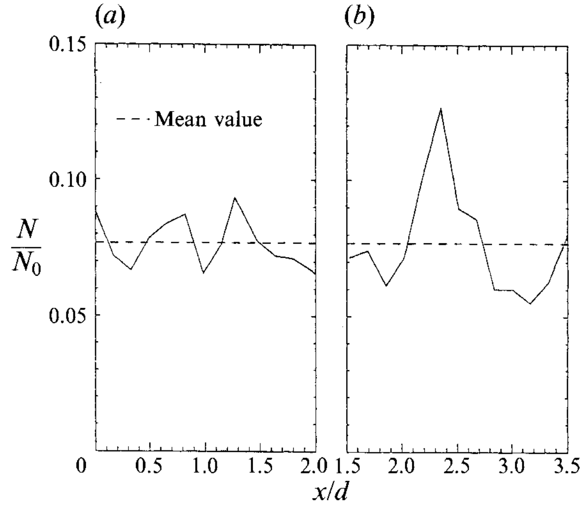

FIGURE 25. Bubble distributions as a function of x/d. Values indicate the number of bubbles within a $\Delta x/d = 0.164$ wide section (a hologram is divided into 13 sections), divided by the total number of bubbles in a hologram. (*a*) The trigger is at $x/d = 1.25$; $r/d = 1.5$ (same data as figure 24*a*). (*b*) The trigger is at $x/d = 2.5$; $r/d = 1.5$ (same data as figure 24*c*).

an increase in σ_i. For most of his nozzles, however, the inception index decreases with increasing velocity. The latter trend is not 'universal', and in other cases involving free shear layers, such as axisymmetric flows behind a sharp-edged disk (Kermeen & Parkin 1957) and around a blunt circular cylinder (Katz 1984), the cavitation index increases with velocity (Reynolds number). We cannot explain this contradiction. As a final niche on this issue, it should be noted that owing to self-induced motion (Saffman 1992), the convection velocity of a vortex ring with diameter d, circulation $V_j \lambda$, and core radius r_c is approximately equal to $(V_j \lambda / 2\pi d)[\ln(4d/r_c) - \frac{1}{4} + \theta(4r_c/d)^2]$. Thus, unlike two-dimensional shear layers, the motion of a ring depends on λ/d and d/r_c. This is another scale effect.

4. Distributions of bubbles and probability of cavitation inception

4.1. *Probability of inception in the near field*

As argued in §1, cavitation inception requires exposure of a microscopic nucleus to a sufficiently low pressure. Thus, the likelihood of inception depends on the probability and spatial distributions of pressure peaks, as well as the spatial distribution of bubbles. A simplified estimate for the probability of inception at a specific cavitation index, $\mu(\sigma = \sigma_i, x, r)$, is:

$$\mu(\sigma = \sigma_i, x, r) = \mu(p \leqslant p_v - 4s/3R, x, r)\,\mu(R, x, r), \tag{13}$$

where $\mu(p \leqslant p_v - 4s/3R, x, r)$ is the probability that the pressure is sufficiently low, and $\mu(R, x, r)$ is the probability of finding a bubble at the same site. By using this expression, it is assumed that the pressure field and the distribution of bubbles are independent. This assumption is wrong, since the bubbles migrate into regions with low pressure, and slip velocities in the order of 10% of the local velocity have been observed. The impact of this dependence on $\mu(R, x, r)$ is very difficult to compute, but it should be in the same order as the relative magnitude of the slip velocity.

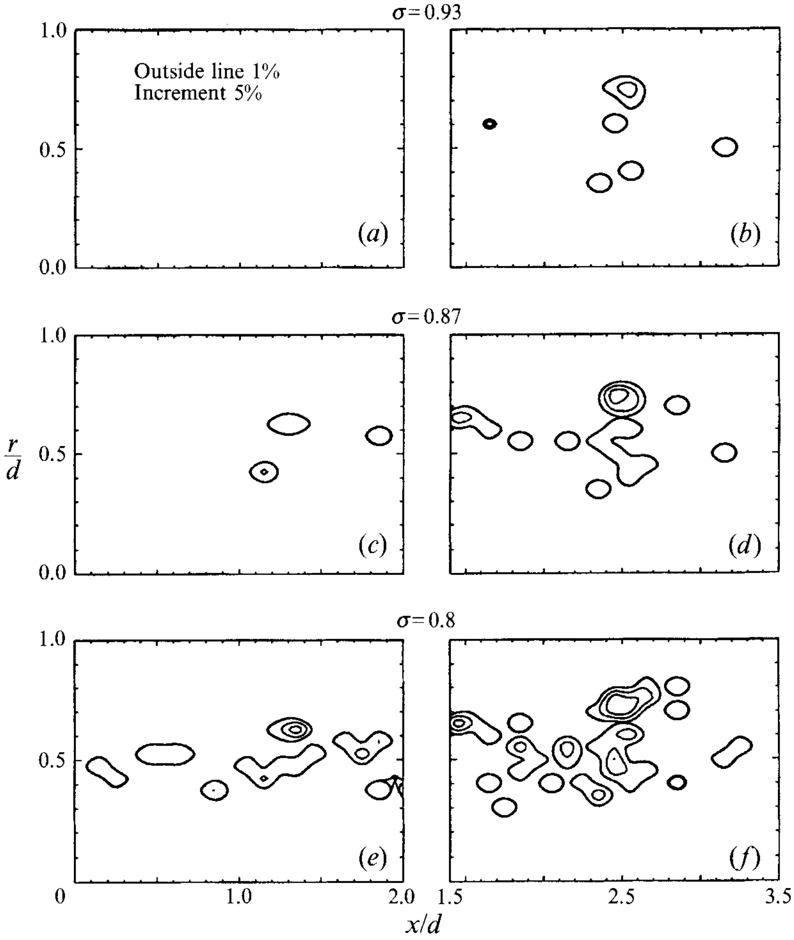

FIGURE 26(a–f). For caption see facing page.

The value of $\mu(p \leqslant p_v - 4s/3R, x, r)$ can be determined for every section of the flow field, by using the probability histogram of pressure peaks (similar to figures 15, 16, 22 and 23). The probability of finding a bubble at a specific location is also available from the experimental results, at least for the present test conditions. Phase averaged spatial distributions of bubbles, determined from the data used for computing the pressure, are presented in figure 24. Each plot presents the fraction of bubbles within a region with size $\Delta x/d = 0.164$ and $\Delta r/d = 0.04$. The results confirm that there is a considerable reduction in dispersion due to acoustic excitation. In general, regions with high bubble concentrations are not necessarily the sites of cavitation inception. However, there is a clear local population peak around $x/d = 2.5$ and $r/d = 0.7$ (figure 24b), the main site of high negative pressure peaks (figure 13). Further illustration of the non-uniform distribution of bubbles is demonstrated in figure 25. It shows the phase averaged density of bubbles as a function of x/d, namely the integral along r/d of the data in figure 24. There is a clear increase in density at the sites of the trigger transducer at $x/d = 1.25$ and 2.5. Thus, an assumption of uniform bubble distribution within the jet would undoubtedly lead to a considerable error. To estimate the probability of finding a bubble in any region, we divide the number of holograms containing bubbles at that site by the total number of holograms recorded. In other words, $\mu(R, x, r)$ can be

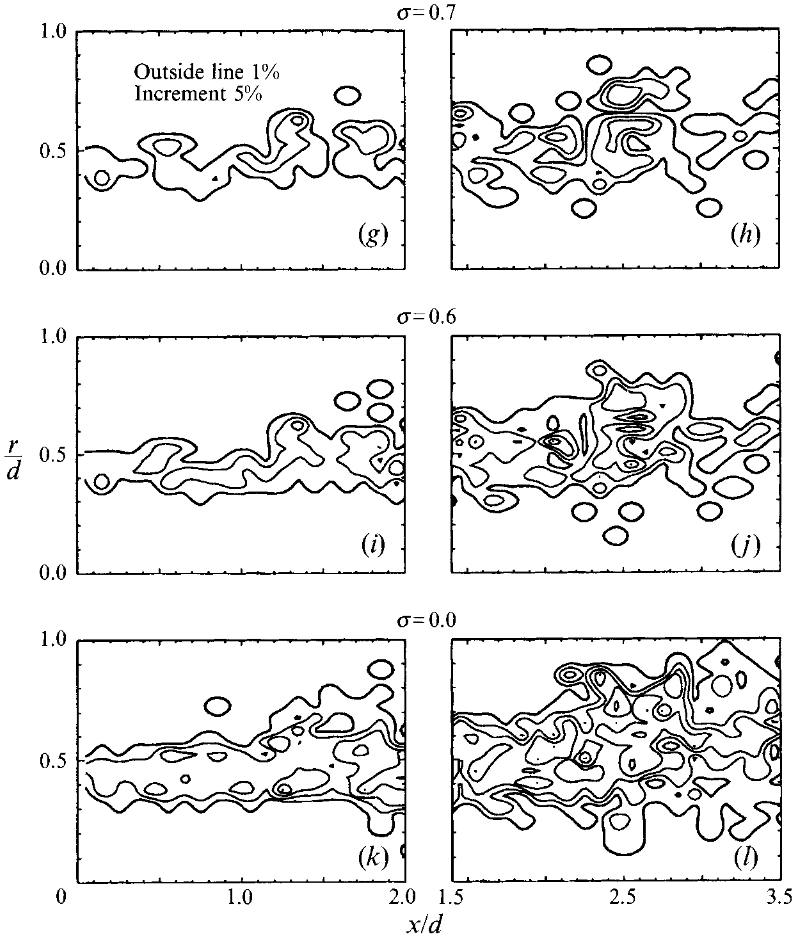

FIGURE 26. Contour plots of the probability of cavitation inception within $0 < x/d < 3.5$; $0 < r/d < 1.0$. In (*a*), (*c*), (*e*), (*g*), (*i*) and (*k*): the trigger transducer is at $x/d = 1.25$; $r/d = 1.5$. In (*b*), (*d*), (*f*), (*h*), (*j*) and (*l*): the trigger transducer is at $x/d = 2.5$; $r/d = 1.5$.

evaluated from figure 24 by multiplying the indicated values by the total number of bubbles, and dividing by the number of holograms (40 for the unexcited jet). The result still differs slightly from the actual probability, since in some cases (about 10%) a single hologram contains more than one bubble in the same region.

Since both terms in (12) are known, the probability for cavitation inception at any site as a function of σ can be computed. Sample probabilities, computed for regions defined by $\Delta x/d = 0.1$ and $\Delta r/d = 0.05$, are presented in figure 26. It is evident that the region susceptible to cavitation inception, and the likelihood in each region, increase with decreasing σ. The preferred sites at high σ are consistent with the present measurements, samples of which are shown in figure 6. When $\sigma > 0.9$ cavitation occurs only in the vortex pairing region, and as σ is reduced below 0.8, it occurs also at $x/d = 1.25$. Note that cavitation does not appear in all the holograms at the same conditions, and the results presented in figure 26 are quite realistic. However, we did not record enough holograms to perform a reliable comparison to the computed probabilities.

By using the available data, it is also possible to estimate the probability of a single cavitation event, $\overline{\mu(\sigma=\sigma_i)}$, for the entire near field of the jet ($0 < x/d < 3.5$), from the following equation:

$$\overline{\mu(\sigma=\sigma_i)} = 1 - \prod_m \prod_n [1 - \mu(\sigma = \sigma_i, x_n, r_m)]. \tag{14}$$

Again, by using (14) it is assumed that the probabilities in different regions are independent, which is obviously wrong. Consequently, the results presented in figure 27 have only a qualitative value. For comparison, we also present probabilities computed with uniform bubble density over the entire jet (equal to the mean density), and uniform bubble flux in the shear layer (density decreasing with increasing x/d as the shear layer grows). It is evident that the non-uniform, actual distribution almost doubles the probability of inception at $\sigma = 0.93$, compared to the results obtained with a uniform flux. The difference diminishes below $\sigma = 0.84$, and the trend reverses (but with a small difference) at lower σ, as major portions of the jet become susceptible to cavitation (figure 26). Thus, even when the jet is seeded with a fairly high concentration of bubbles, $\overline{\mu(\sigma=\sigma_i)}$ is still quite sensitive to their spatial distributions. Trends in unseeded flows will be discussed shortly.

An appropriate timescale is missing in (13) and (14) since we use phase averaged pressure and bubble distributions, and the results are relevant for a specific 'flow configuration'. This pattern is unsteady and would change if a different location were chosen for the trigger transducer, particularly in the vortex pairing region. Consequently, the local and overall probabilities are also likely to change. Since the processes are strongly correlated during a cycle, it is even inappropriate to repeat the entire measurements for a series of different 'flow configurations', and determine the total probability per cycle, $\overline{\mu(\sigma=\sigma_i, T)}$, from:

$$\overline{\mu(\sigma=\sigma_i, T)} = 1 - \prod_{n=1}^{T/\Delta t} [1 - \overline{\mu(\sigma=\sigma_i, n\Delta t)}]. \tag{15}$$

Here T is the pairing timescale, which according to the pressure spectra is about 6 ms, and $\overline{\mu(\sigma=\sigma_i, n\Delta t)}$ is the result of (14) for a specific flow configuration (identified by $n\Delta t$, where n varies between 1 and $T/\Delta t$). Other possible (and more appropriate) approaches should involve use of measured temporal correlations to determine the proper Δt, over which one can assume that the processes become independent. It is also possible to estimate Δt as $\Delta x/V_j$, where Δx is the spatial distance required for achieving statistical independence. These issues are beyond the scope of the present paper and will be dealt with in future studies.

4.2. *Probability of inception beyond the potential core*

Probabilities of inception for the region located beyond the end of the potential core, where macroscopic cavitation occurs, are presented in figure 28. Dominated by differences in $\mu(p \leqslant p_v - 4s/3R)$, as shown in figure 23, the previously discussed trend, namely that the inception index decreases with increasing velocity, is also evident here. Note that in most cases, unless the jet is carefully seeded from its centreline (as done in figure 5*d*), there is already a considerable level of microscopic cavitation in the shear layer upstream (figures 5*b*, *c*). Consequently, it is likely that under normal circumstances, the population of bubbles in this region is substantially higher than the free stream. To demonstrate the effect of such an increase, we also include a hypothetical probability distribution, computed with five times the measured nuclei density. The impact on $\overline{\mu(\sigma=\sigma_i)}$ is evident, especially at high cavitation indices. Figure 28 contains also a comparison to the probability of inception computed with an

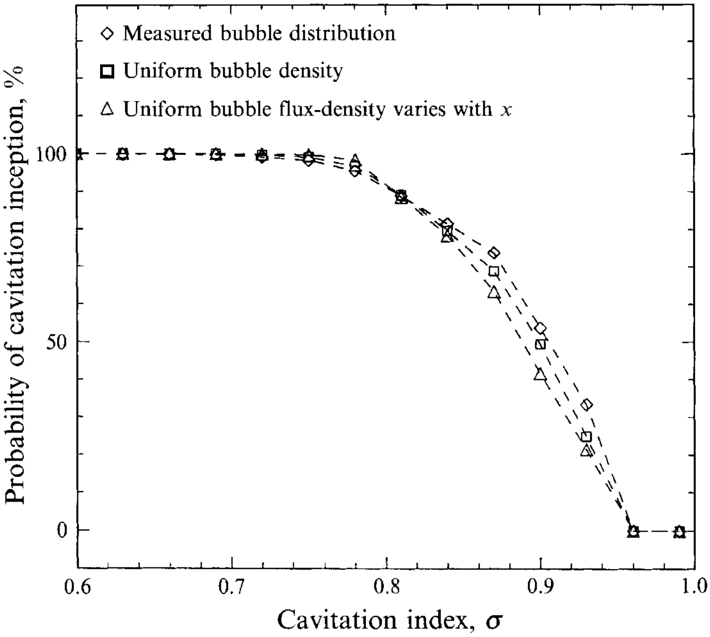

FIGURE 27. Probability of cavitation inception within the near field of the jet ($0 < x/d < 3.5$; $0 < r/d < 1.2$). Effects of the actual non-uniform density is demonstrated by comparison to results obtained with a uniform density and uniform flux of bubbles.

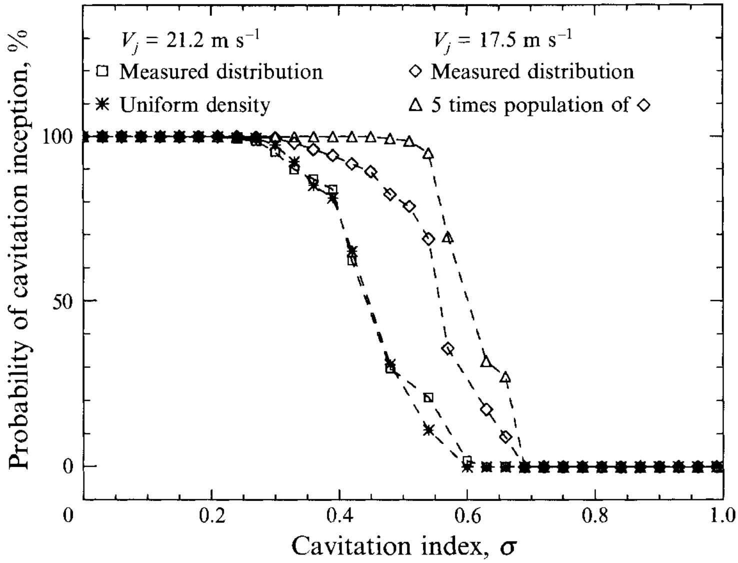

FIGURE 28. Probability of cavitation inception near the end of potential core ($4 < x/d < 6.5$; $0 < r/d < 0.65$), at jets velocities of 17.5 m s^{-1} and 21.2 m s^{-1}. Results obtained with the actual non-uniform density are compared to a uniform distribution at the same density, as well as to a higher bubble population.

assumed uniform bubble density, but with the same total flux. Even for the present case, for which the measurements do not involve any conditional sampling, $\overline{\mu(\sigma = \sigma_i)}$ computed with the actual population is still higher. Thus, the spatial distribution of bubbles clearly depends on the pressure distribution. Similarly to the discussion in §4.1,

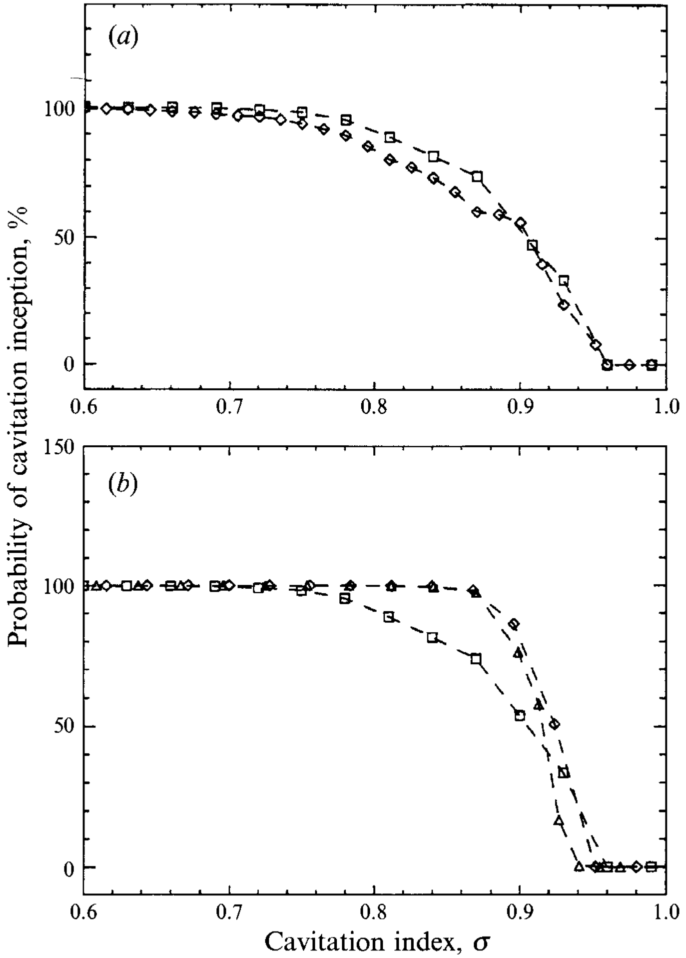

FIGURE 29. Probability of cavitation inception. (*a*) A comparison between excited and unexcited jets. Measured bubble distribution: □, without excitation; ◇, with excitation. (*b*) A comparison to the probability of inception in unseeded water containing typical free-stream bubble distribution. Bubble distribution: □, present experiment; △, O'Hern (1987); ◇, O'Hern corrected for changes in diameter following entrainment by the jet.

the present measurements do not provide appropriate timescales. However, crude spatial correlations for the instantaneous data suggest that the correlation becomes small when $\Delta x/d \approx 0.5$. Thus, a reasonable choice for a timescale is $\Delta t \approx \Delta x/v_j \approx 0.5d/V_j$, namely 0.6 and 0.7 ms for 17.5 and 21.2 m s^{-1} jets, respectively. An expression similar to (15) can then be used for introducing the time into the present estimates.

4.3. *Probability of inception in an excited jet and unseeded flows*

As previously observed, and figure 29(*a*) confirms, acoustic excitation has little effect on the overall probability of inception at high σ (figure 29*a*). There is a slight difference at $\sigma < 0.88$, primarily since the excited jet has less sites of low pressure at $x/d < 2.0$.

In unseeded flows, where most measurements have been performed in the past, the distributions of free-stream bubbles vary significantly, and depend on experimental procedures, dissolved air content, etc. Selecting O'Hern's (1987) results as a typical distribution, the densities of bubbles with mean diameters of 40 μm and 80 μm are about 3 and 0.07 bubbles cm^{-3}, respectively (the present density is about 1.7 bubbles cm^{-3}). However, when these bubbles are entrained into the jet, their sizes change even prior to cavitation, owing to exposure to a lower pressure within the shear-layer vortices. The change can be significant. For example, if $P_0 = 26$ p.s.i. the phase averaged minimum pressure can be as low as 4 p.s.i., and consequently a 40 μm bubble can grow up to about 75 μm. Thus, the free-stream distribution should be corrected based on the phase averaged pressure and using (8). Assuming a uniform bubble density (as we already know, this assumption is incorrect, and is introduced here solely for the purpose of demonstrating other trends), it is then possible to estimate the probability of cavitation inception. The results are compared in figure 29(*b*) to the probability of inception in the present jet, as well as to a probability computed assuming that the bubble diameter remains unchanged following entrainment by the jet. Owing to the larger size of bubbles in the present experiments, the magnitudes of $-4s/3R$ are smaller, and as a result $\mu(\sigma = \sigma_i)$ at $\sigma \geqslant 0.95$ is higher. However, at lower σ the probabilities computed with the corrected O'Hern's distributions, exceed the present results. The difference increases with decreasing σ, as larger portion of the jet containing the assumed uniform high bubble density become susceptible to cavitation. If we do not account for the change in bubble size, $\mu(\sigma = \sigma_i)$ is considerably lower at $\sigma \geqslant 0.86$, mainly due to differences in the values of $-4s/3R$.

5. Conclusions

Instantaneous and phase averaged pressure distributions in the near field of a jet, and their effects on the conditions for the onset of cavitation were investigated. The measurements were performed by using microscopic bubbles as pressure sensors, and holography as a means of detecting them. The lowest negative pressure coefficients, ranging between -0.9 and -1.0, were measured in the core of the vortex rings during pairing. The lowest level prior to pairing was in the -0.8 and -0.9 range. These measurements were consistent with the observed conditions and location of cavitation inception. However, although the population of bubbles increased as a result of cavitation, they remained very small (less than 0.5 mm in diameter), and could only be detected by examining the holograms as well as from the signal of the trigger transducer. Weak acoustic excitation changes the location of the shear-layer vortices, and seemed to eliminate (or delay) the pairing process. However, the magnitude of pressure peaks, and the conditions for cavitation inception did not change significantly. Tripping of the boundary layer in the nozzle did not have a significant effect on the onset of cavitation.

Downstream of the potential core ($x/d > 5$), where macroscopic cavitation (visible under stroboscopic light) started, the magnitudes of pressure peaks were considerably lower (~ -0.6). Although the r.m.s. values did not vary with velocity, the magnitudes and likelihood of high negative peaks, as well as the cavitation inception indices decreased with increasing velocity. We cannot explain this phenomenon without unfounded speculations.

By using the probability distributions of pressure peaks, and the measured spatial distributions of bubbles, it was possible to estimate the local probability of cavitation inception at every point, as well as the overall probability within the entire near field of the jet. The analysis demonstrated that migration of bubbles into low-pressure regions increased the likelihood of cavitation inception. Other trends were also confirmed, including the effect of acoustic excitation, jet speed, and examined the impact of other bubble distributions.

This project was sponsored by the Office of Naval Research, under grant no. N00014-91-J-1176. Funding for purchasing the holocamera was provided by an NSF Engineering Research Equipment grant no. MSM-8705120. The high-speed jet cavitation facility was constructed with funds provided under NSF grant no. MSM-851065. Their support is gratefully acknowledged.

REFERENCES

ARNDT, R. E. A. 1981 Cavitation in fluid machinery and hydraulic structures. *Ann. Rev. Fluid Mech.* **13**, 273–328.

ARNDT, R. E. A. & GEORGE, W. K. 1978 Pressure fields and cavitation in turbulent shear flows. In *12th Symp. on Naval Hydrodynamics, Washington DC*, pp. 327–339.

BALL, J. W. 1960 Discussion to Reference 75. *Trans. ASME* I: *J. Fluids Engng* **84** (1), 6–11.

BAKER, C. B., HOLL, J. W. & ARNDT, R. E. A. 1975 The influence of gas content and polyethylene oxide additive upon confined jet cavitation in water. *TM* 75-274. Applied Research Laboratory, Pennsylvania State University.

BAREFOOT, G. L. 1972 Fluctuating pressure characteristics in the mixing region of a perturbed and unperturbed round free jet. *TM* 72-165. Applied Research Laboratory, Pennsylvania State University.

BILLET, M. L. 1985 Cavitation nuclei measurements – a review. *ASME Cavitation and Multiphase Flow Forum, Albuquerque, NM.* FED vol. 23, pp. 31–38.

CECCIO, S. L. & BRENNEN, C. E. 1991 Observations of the dynamics and acoustics of travelling bubble cavitation. *J. Fluid Mech.* **223**, 633–660.

COLLIER, R. J., BURKHARDT, C. B. & LIN, L. H. 1970 *Optical Holography*. Academic.

FUCHS, H. V. 1972 Measurements of pressure fluctuations within subsonic turbulent jets. *J. Sound Vib.* **22** (1), 361–378.

GEORGE, W. K., BEUTHER, P. D. & ARNDT, R. E. 1984 Pressure spectra in turbulent free shear flows. *J. Fluid Mech.* **148**, 155–191.

GREEN, S. I. 1988 Tip vortex – single phase and cavitating flow phenomena. PhD thesis (Eng. 183-17), California Institute of Technology.

HO, C. M. & HUERRE, P. 1984 Perturbed free shear layers. *Ann. Rev. Fluid Mech.* **16**, 365–424.

HUSSAIN, A. K. M. F. 1986 Coherent structure and turbulence. *J. Fluid Mech.* **173**, 303–356.

HUSSAIN, A. K. M. F. & ZAMAN, K. M. B. 1980 Vortex pairing in a circular jet under controlled excitation. Part 2. Coherent structure dynamics. *J. Fluid Mech.* **101**, 39–71.

HUSSAIN, A. K. M. F. & ZAMAN, K. M. B. 1981 The preferred mode of an axisymmetric jet. *J. Fluid Mech.* **110**, 39–71.

HUSSAIN, A. K. M. F. & ZEDAN, M. F. 1978 Effects of the initial condition on the axisymmetric free shear layer: effects of the initial momentum thickness. *Phys. Fluid* **21**, July, 1100–1112.

JOHNSON, V. E., CHAHINE, G. L., LINDENMUTH, W. T., CONN, A. F., FREDERICK, G. S. & GIACCHINO, G. J. 1982 Cavitating and structured jets for mechanical bits to increase drilling rate. *ASME paper* no. 82-Pet-13, Energy Sources Technology Conference and Exhibition, March 7–10, New Orleans, LA.

JORGENSEN, D. W. 1961 Noise from cavitating submerged water jets. *J. Acoust. Soc. Am.* **33**, 1334–1338.

KATZ, J. 1984 Cavitation phenomena within regions of flow separation. *J. Fluid Mech.* **140**, 497–536.

KATZ, J. & O'HERN, T. J. 1986 Cavitation in large scale shear flows. *Trans ASME* I: *J. Fluids Engng* **108**, 373–376.

KERMEEN, R. W. & PARKIN, B. R. 1957 Incipient cavitation and wake flow behind sharp-edged disks. *Cal. Inst. Tech., Hydrodyn. Lab. Rep.* 85-4.

KOBAYASHI, R. 1967 Effect of cavitation on the discharge coefficient of standard flow nozzles. *Trans. ASME* D: *J. Basic Engng* **89** (3), 677–685.

LIENHARD, J. H. & GOSS, C. D. 1971 Influence of size and configuration on cavitation in submerged orifice flow. *ASME Paper* 1-FE-39.

Lienhard, J. H. & Stephenson, J. M. 1966 Temperature and scale effects upon cavitation and flashing in free and submerged jets. *Trans. ASME* D: *J. Basic Engng* **88**, 525–532.

Lin, H. J. & Katz, J. 1988 Occurrence of cavitation in water jets. *Liquid Metal Flow: MHD and Application, Progress in Astronautics and Aeronautics*, vol. 111, pp. 585–604.

Meyer, R. S., Billet, M. L. & Holl, J. W. 1992 Freesteam nuclei and traveling-bubble cavitation. *Trans. ASME* I: *J. Fluids Engng* **114** (4), 672–679.

Numachi, F., Yamabe, M. & Oba, R. 1960 Cavitation effect on the discharge coefficient of the sharp-edged orifice plate. *Trans. ASME* D: *J. Basic Engng* **84** (1), pp. 1–6.

O'Hern, T. J. 1987 Cavitation inception scale effects: I. nuclei distributions in natural waters; II. cavitation inception in turbulent shear flow. PhD thesis (Eng. 183–15), California Institute of Technology.

Ooi, K. K. 1981 Scale effects on cavitation inception in submerged jets. PhD thesis (183–6), California Institute of Technology.

Ooi, K. K. & Acosta, A. J. 1983 The utilization of specially tailored air bubbles as static pressure sensors in a jet. *Trans. ASME* I: *J. Fluids Engng* **106** (4), 459–465.

Pauchet, J., Retailleau, A. & Woillez, J. 1992 The prediction of cavitation inception in turbulent water jets. In *ASME Cavitation and Multiphase Flow Forum*, FED vol. 135, pp. 149–158.

Plesset, M. S. & Prosperetti, A. P. 1977 Bubble dynamics and cavitation. *Ann. Rev. Fluid Mech.* **9**, 145–185.

Ramani, D. & Chahine, G. L. 1992 Analytical study of a gas bubble in the flow field of a line vortex. In *ASME Cavitation and Multiphase Flow Forum*, FED vol. 135, pp. 69–76.

Ran, B. & Katz, J. 1991 The response of microscopic bubbles to sudden changes in ambient pressure. *J. Fluid Mech.* **111**, pp. 585–604.

Saffman, P. G. 1992 *Vortex Dynamics*. Cambridge University Press.

Sridhar, G. & Katz, J. 1991 Implementation of particle image velocimetry to multi-phase flows. In *ASME Cavitation and Multiphase Flow Forum*, FED vol. 109, pp. 204–209.

Willmarth, W. W. 1975 Pressure fluctuations beneath turbulent boundary layers. *Ann. Rev. Fluid Mech.* **7**, 13–38.

Zaman, K. M. B. & Hussain, A. K. M. F. 1980 Vortex pairing in circular jet under controlled excitation. *J. Fluid Mech.* **101**, 449–491.